







ALMA observations of the Extended Green Object G19.01–0.03 – II. A massive protostar with typical chemical abundances surrounded by four low-mass pre-stellar core candidates

G. M. Williams ^{1,★}, C. J. Cyganowski ², C. L. Brogan ³, T. R. Hunter ³, P. Nazari ⁴
and R. J. Smith ^{2,5}

¹*School of Physics & Astronomy, The University of Leeds, Leeds LS2 9JT, UK*

²*Scottish Universities Physics Alliance (SUPA), School of Physics and Astronomy, University of St Andrews, North Haugh, St Andrews KY16 9SS, UK*

³*National Radio Astronomy Observatory (NRAO), 520 Edgemont Rd, Charlottesville, VA 22903, USA*

⁴*Leiden Observatory, Leiden University, PO Box 9513, NL-2300 RA Leiden, the Netherlands*

⁵*Jodrell Bank Centre for Astrophysics, Department of Physics and Astronomy, University of Manchester, Oxford Road, Manchester, M13 9PL, UK*

Accepted 2023 September 2. Received 2023 September 2; in original form 2023 February 22

ABSTRACT

We present a study of the physical and chemical properties of the Extended Green Object (EGO) G19.01–0.03 using sub-arcsecond angular resolution Atacama Large Millimetre/submillimetre Array (ALMA) 1.05 mm and Karl G. Jansky Very Large Array (VLA) 1.21 cm data. G19.01–0.03 MM1, the millimetre source associated with the central massive young stellar object (MYSO), appeared isolated and potentially chemically young in previous Submillimetre Array observations. In our ~ 0.4 arcsec-resolution ALMA data, MM1 has four low-mass millimetre companions within 0.12 pc, all lacking maser or outflow emission, indicating they may be pre-stellar cores. With a rich ALMA spectrum full of complex organic molecules, MM1 does not appear chemically young, but has molecular abundances typical of high-mass hot cores in the literature. At the 1.05 mm continuum peak of MM1, $N(\text{CH}_3\text{OH}) = (2.22 \pm 0.01) \times 10^{18} \text{ cm}^{-2}$ and $T_{\text{ex}} = 162.7^{+0.3}_{-0.5} \text{ K}$ based on pixel-by-pixel Bayesian analysis of LTE synthetic methanol spectra across MM1. Intriguingly, the peak $\text{CH}_3\text{OH } T_{\text{ex}} = 165.5 \pm 0.6 \text{ K}$ is offset from MM1's millimetre continuum peak by 0.22 arcsec $\sim 880 \text{ au}$, and a region of elevated $\text{CH}_3\text{OH } T_{\text{ex}}$ coincides with free-free VLA 5.01 cm continuum, adding to the tentative evidence for a possible unresolved high-mass binary in MM1. In our VLA 1.21 cm data, we report the first $\text{NH}_3(3,3)$ maser detections towards G19.01–0.03, along with candidate 25 GHz $\text{CH}_3\text{OH } 5(2, 3) - 5(1, 4)$ maser emission; both are spatially and kinematically coincident with 44 GHz Class I CH_3OH masers in the MM1 outflow. We also report the ALMA detection of candidate 278.3 GHz Class I CH_3OH maser emission towards this outflow, strengthening the connection of these three maser types to MYSO outflows.

Key words: masers – techniques: interferometric – stars: formation – stars: individual: G19.01–0.03 – stars: massive – stars: protostars.

1 INTRODUCTION

High-mass stars ($M_* > 8 M_\odot$) are influential in the dynamical and chemical evolution of the interstellar medium (ISM), through their strong feedback, outflows and jets, and through enrichment of the ISM with heavy elements (e.g. Peters et al. 2017; Rosen & Krumholz 2020; Mignon-Risse, González & Commerçon 2021; Grudić et al. 2022). Constraining exactly how high-mass stars form, however, is hampered by their natal molecular clouds being significantly more distant ($d > 1 \text{ kpc}$) and more clustered ($n_* > 100 \text{ pc}^{-3}$) than those of their low-mass counterparts ($M_* < 8 M_\odot$). Furthermore, the short pre-main sequence lifetimes ($< 1 \text{ Myrs}$; Mottram et al. 2011) of high-mass stars ensures that the entirety of their formation is obscured in regions of high

extinction (e.g. Chevance et al. 2020; Kim et al. 2021). Now with the advent of facilities capable of high-angular resolution observations in the (sub)millimetre such as the Atacama Large Millimetre/(sub)millimetre Array (ALMA), we have the ability to resolve and disentangle the thermal emission of the early stages of high-mass star formation.

The core-fed theory of massive star formation (McKee & Tan 2003; Tan et al. 2014) describes the monolithic collapse of virialized high-mass pre-stellar cores that have ceased accreting material from their surroundings and are supported against fragmentation into low-mass cores by magnetic and turbulent pressures. In this picture, high-mass pre-stellar cores (e.g. Motte et al. 2007) – starless and self-gravitating structures thought to form in infrared dark clouds (IRDCs; Rathborne, Jackson & Simon 2006; Peretto & Fuller 2009) – are the earliest stage of massive star formation. Observationally, however, very few candidates of truly quiescent high-mass pre-stellar cores

* E-mail: williamsgwen12@gmail.com

exist (e.g. Cyganowski et al. 2014; Duarte-Cabral et al. 2014; Wang et al. 2014; Kong et al. 2017; Nony et al. 2018; Cyganowski et al. 2022; Barnes et al. 2023), suggesting they may either be very short lived (e.g. Motte et al. 2007; Kauffmann, Pillai & Goldsmith 2013; Sanhueza et al. 2019), or not exist at all (e.g. Motte, Bontemps & Louvet 2018).

High-mass protostars (or massive young stellar objects, MYSOs; e.g. Hoare et al. 2005; Urquhart et al. 2008) are instead widely associated with active star formation signatures such as 6.7 GHz CH_3OH , 22 GHz H_2O , and $\text{NH}_3(3,3)$ masers (e.g. Pillai et al. 2006; Urquhart et al. 2011; Brogan et al. 2019; Jones et al. 2020; Towner et al. 2021). Signatures of ongoing accretion are also prevalent towards MYSOs, such as high-velocity bi-polar outflows (e.g. Beuther et al. 2002; Duarte-Cabral et al. 2013; Yang et al. 2022) and less commonly circumstellar accretion discs (e.g. Beltrán et al. 2014; Johnston et al. 2015; Ilee et al. 2016; Cesaroni et al. 2017; Maud et al. 2018; Dewangan et al. 2022). MYSOs are typically observed to have strong (sub)millimetre continuum, and a sub-population of MYSO(s) – classed as Extended Green Objects (EGOs; Cyganowski et al. 2008, 2009) – exhibit extended 4.5 μm emission attributed to shocks in outflows driven by the central MYSO(s). Many of these EGOs only exhibit weak centimetre continuum emission (Cyganowski et al. 2011b; Towner et al. 2021). The clump-fed theory of massive star formation (Bonnell et al. 2001; Smith, Longmore & Bonnell 2009) describes the competitive accretion of clusters of initially low-mass star progenitors. High-mass star progenitors develop through the continued accretion of material by protostellar sources that find themselves at the centre of the gravitational potential of the cluster. This requirement for a continually accreting protocluster in the clump-fed theory is a key factor that distinguishes it from the monolithic core-fed theory and is a crucial observable for constraining models of early massive star formation (e.g. Cyganowski et al. 2017; Issac et al. 2020; Law et al. 2022).

Complex organic molecules (COMs) are molecular species that contain at least one carbon atom and a total of at least six atoms (Herbst & van Dishoeck 2009). They are thought to form on dust grain surfaces during both the cold collapse and ‘warm-up’ phases of massive star formation (e.g. Garrod & Herbst 2006; Garrod 2013; Öberg 2016; Garrod et al. 2022), with COMs forming earlier and at lower temperatures in models including non-diffusive chemistry (Garrod et al. 2022). In general, in gas–grain astrochemical models radiative heating from MYSOs ultimately heats the grains enough to sublimate their ice mantles, releasing both COMs and simpler molecules into the gas phase where they are observable via (sub)millimetre wavelength spectral-line emission (e.g. Öberg 2016; Garrod et al. 2022, and references therein). While COMs can also be produced by gas-phase mechanisms, production on grains dominates in recent models (e.g. Garrod et al. 2022). MYSOs that are characterized by a forest of molecular lines in the (sub)millimetre are classed as hot cores (e.g. Sánchez-Monge et al. 2017; Sewilo et al. 2018; Liu et al. 2021) and typically have temperatures that exceed 100 K (e.g. Öberg 2016). Later in the evolution of the system (though not necessarily independent of the hot core stage), hypercompact (HC) HII regions form, signposted by centimetre continuum due to the ionization of the surrounding material by the high-mass protostar(s) (e.g. Kurtz 2005; Yang et al. 2019, 2021). With the exquisite sensitivities achievable by ALMA in the (sub)millimetre and the Karl G. Jansky Very Large Array (VLA) in the centimetre, combined studies of both the chemical and physical properties of massive star progenitors and their environments are now possible.

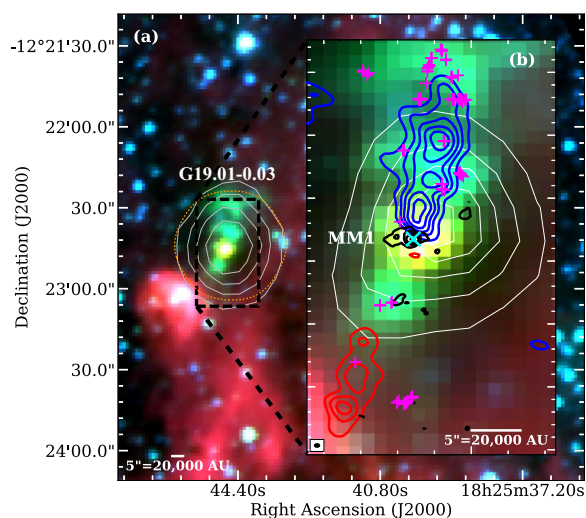


Figure 1. *Spitzer* GLIMPSE three-colour image (RGB: 8.0, 4.5, and 3.6 μm). (a) The dotted orange contour marks the 30 per cent response level of the ALMA mosaic, designed to encompass the full extent of the ATLASGAL clump. ATLASGAL 870 μm emission contours are shown in grey (at 12σ , 16σ , 20σ , and 24σ , where $\sigma = 0.08 \text{ Jy beam}^{-1}$; Schuller et al. 2009, 18 arcsec resolution). The zoomed inset of (b) is shown by the dashed black box. (b) High-velocity blue- and red-shifted SMA $^{12}\text{CO}(2-1)$ emission contours are shown in blue (7.2, 12.0, 15.6, 19.2, and 22.8 $\text{Jy beam}^{-1} \text{ km s}^{-1}$) and red (4.8, 7.2, and 9.6 $\text{Jy beam}^{-1} \text{ km s}^{-1}$), respectively (Cyganowski et al. 2011a), and ALMA 1.05 mm continuum contours are shown in black (0.00125, 0.004, 0.016, and 0.200 Jy beam^{-1} ; Williams et al. 2022). Magenta +’s mark the VLA positions of 44 GHz Class I CH_3OH masers (Cyganowski et al. 2009), and the cyan \times marks the intensity-weighted VLA 6.7 GHz Class II CH_3OH maser position from Williams et al. (2022). Herschel PACS 70 μm emission (Poglitsch et al. 2010) of the HI-GAL clump (Elia et al. 2017) is plotted with white contours (2.5, 4.5, 6.5, 8.5, and 10.5 Jy pixel^{-1}). The PACS 70 μm beam is 6 arcsec \times 12 arcsec (FWHM ~ 8 arcsec; Herschel Explanatory Supplement Volume III 2017). The ALMA beam is plotted in the bottom left.

1.1 Target: EGO G19.01–0.03

The EGO G19.01–0.03 (hereafter G19.01) is an intriguing example of early massive star formation. As in Williams et al. (2022), we adopt $D = 4.0 \pm 0.3$ kpc, the near kinematic distance estimated using the Galactic rotation curve parameters of Reid et al. (2014) and the NH_3 LSRK velocity from Cyganowski et al. (2013). As shown in Fig. 1, emission from the surrounding clump is detected in the HI-GAL and ATLASGAL surveys; the clump is also detected at 1.1 mm by the Bolocam Galactic Plane Survey (Rosolowsky et al. 2010). The clump mass is $\sim 1000 M_{\odot}$: the HI-GAL catalogue of Elia et al. (2017) reports a clump mass, radius, and temperature of $974 M_{\odot}$, 0.16 pc, and 17.9 K, respectively for $D = 3.658$ kpc ($\sim 1165 M_{\odot}$ and 0.18 pc scaled to $D = 4.0$ kpc) while Schuller et al. (2009) report a clump mass of $1070 M_{\odot}$ for $D = 4.3$ kpc based on the 870 μm ATLASGAL data ($\sim 926 M_{\odot}$ scaled to $D = 4.0$ kpc). Towards the clump, a single millimetre continuum core (hereafter called MM1) is seen in isolation with the submillimetre array (SMA) at 1.3 mm and with the Combined Array for Research in Millimeter-wave Astronomy (CARMA) at 3.4 mm (at 2.4 and 5.4 arcsec angular resolution, respectively; Cyganowski et al. 2011a). MM1 coincides with 6.7 GHz Class II CH_3OH maser emission (Cyganowski et al. 2009) placing it as a massive source (e.g. Urquhart et al. 2013; Billington et al. 2020; Jones et al. 2020) and is seen to drive a highly collimated, high-velocity bi-polar outflow observed with the SMA in $^{12}\text{CO}(2-1)$ and with CARMA in $\text{HCO}^+(1-0)$ and $\text{SiO}(2-1)$ emission (Cyganowski

et al. 2011a). Class I CH₃OH maser emission (44 GHz) is seen to trace the edges of the outflow lobes (Cyganowski et al. 2009). At the sensitivity of the SMA and CARMA data, MM1 exhibited some hot core emission but lacked chemical richness, conspicuously lacking in emission from Oxygen-bearing COMs. Only two COMs were detected (CH₃OH and CH₃CN) with only two lines with excitation temperature > 100 K (Cyganowski et al. 2011a). MM1 was not detected in deep, arcsec-resolution VLA observations at 3.6 and 1.3 cm to 4 σ limits of 0.12 and 1.04 mJy beam⁻¹, respectively (Cyganowski et al. 2011b), suggesting a very low ionizing luminosity capable of producing only a very small HII region. Put together, MM1 appeared as an isolated, high-mass millimetre continuum source, in a state of ongoing accretion, without strong centimetre continuum or rich hot-core line emission. As such, MM1 was until recently considered an excellent candidate for a very early stage of evolution, with potential to shed light on the core-fed theory of high-mass star formation.

The first paper of our ALMA Cycle 2 follow-up study (Williams et al. 2022, hereafter Paper I) presented the highest angular resolution observations of G19.01 to date, at \sim 0.4 arcsec angular resolution in Band 7 at 1.05 mm. With ALMA, MM1 was observed to exhibit a rich millimetre spectrum with a variety of COMs, in contrast to the earlier lower-resolution and sensitivity SMA observations. Kinematic analysis of the strongest, most isolated ALMA-detected molecules revealed the first direct evidence of a rotationally supported accretion disc around MM1 traced by a velocity gradient perpendicular to the bi-polar outflow direction, with an enclosed mass of 40–70 M_⊙ within a 2000 au radius. In conjunction with new VLA observations at 5.01 and 1.21 cm, the centimetre-millimetre spectral energy distribution (SED) was best described by a two-component model, with millimetre emission dominated by thermal dust, and the \sim 5 cm continuum dominated by free-free emission interpreted as a hypercompact HII region, placing MM1 in a later stage of evolution than that concluded with previous observations. Furthermore, the ALMA 1.05 mm continuum revealed for the first time the detection of four neighbouring millimetre sources in the vicinity of MM1, hinting at the possibility of the early stages of protocluster formation.

In this paper (Paper II), we use our ALMA Cycle 2 1.05 mm and VLA 1.21 cm observations to study the chemistry and protocluster environment of G19.01–0.03 MM1 and the properties of the newly detected millimetre sources. In Section 2, we describe the observations; in Section 3, we present the ALMA continuum and molecular line emission, as well as VLA ammonia and methanol emission. In Section 4, we present our modelling of the COM emission, rotation diagram analysis, continuum properties of the millimetre neighbours, and discuss MM1’s chemistry in the context of sources from the literature. We summarize our main conclusions in Section 5.

2 OBSERVATIONS

2.1 Atacama Large Millimetre/submillimetre Array

Our ALMA Cycle 2 observations were designed to search for low-mass cores within the clump-scale gas reservoir associated with G19.01–0.03 MM1: the extent of the ALMA mosaic (\sim 40 arcsec \approx 0.78 pc at $D = 4$ kpc) is shown in Fig. 1 and observing parameters are summarized in Table 1 and below. These observations are also described in detail in Paper I.

For our observations, the ALMA correlator was configured to cover seven spectral windows (spws), including five narrow spws targeting particular spectral lines and two wide spws. Details of

Table 1. Observing parameters for ALMA 1.05 mm and VLA 1.21 cm data.

Parameter	ALMA 1.05 mm	VLA 1.21 cm
Observing date	2015 May 14	2013 November 11–12
Project code (PI)	2013.1.00812.S (C. Cyganowski)	13B-359 (T. Hunter)
Gain calibrator	J1733–1304	J1832–1035
Bandpass calibrator	J1733–1304	J1924–2914
Flux calibrator	Titan ^a	J1331 + 3030
On-source integration time	44 min	139 min
Number of antennas	37	25
Antenna configuration	C43-3/(4)	B
Phase Centre (J2000):		
R.A. (h m s)	18:25:44.61 ^b	18:25:44.80
Dec. (° ′ ″)	–12:22:44.00 ^b	–12:22:46.00
Projected baseline lengths	20–533 m 19–508 k λ	0.14–9.98 km 12–825 k λ
Mean frequency ^c	285.12 GHz	24.81 GHz
Mean wavelength ^c	1.05 mm	1.21 cm
Number of pointings	7	1
Field of view ^{c, d}	\sim 40 arcsec	1.8 arcmin
Synthesized beam ^c	0′.52 \times 0′.35	0′.33 \times 0′.22
Beam position angle ^{c, e}	88.4°	0.5°
Maximum Recoverable Scale ^f	4′.2	4′.5
Continuum rms noise ^g	0.25 mJy beam ⁻¹	6.0 μ Jy beam ⁻¹

^a Using Butler-JPL-Horizons 2012 models.

^b For the central pointing of the mosaic.

^c For the continuum image.

^d ALMA: to 30 per cent level of mosaic response. VLA: primary beam FWHP at mean frequency.

^e Measured East of North, i.e. positive in the anti-clockwise direction.

^f Calculated from the fifth percentile shortest baseline (as stated in the ALMA Technical Handbook) and mean frequency, using `au.estimateMRS` from the `ANALYSISUTILS` Python package.

^g Estimated from emission-free regions within the 30 per cent response level of the ALMA mosaic.

the narrow spws are given in Table 2. The wide spws, with central frequencies of \sim 278.2 and \sim 292.0 GHz, each have a bandwidth of 1.875 GHz, and a Hanning-smoothed spectral resolution of 1.13 MHz (1.156 \times the channel spacing of 0.977 MHz because of online channel averaging in the ALMA correlator).

As detailed in Paper I, the data were calibrated using the CASA 4.2.2 version of the ALMA calibration pipeline and line-free channels were identified using the approach of Brogan et al. (2016) and Cyganowski et al. (2017). These line-free channels were used to construct a pseudo-continuum data set and to perform continuum subtraction in the u, v -plane. For the narrow spw targeting C³³S, this process was problematic due to wide lines and possible absorption (see also Paper I and Cyganowski et al. 2017) and we excluded this spw – which overlaps one of the wide spws in our tuning – from the pseudo-continuum data set and our line analysis. The aggregate continuum bandwidth of the final pseudocontinuum data set is \sim 1.6 GHz. The continuum data were iteratively self-calibrated and were imaged using Briggs weighting with a robust parameter of 0 and multi-frequency synthesis; the key parameters of the resulting image are listed in Table 1. The synthesized beamsizes of the continuum image (0′.52 \times 0′.35) corresponds to a physical scale of 2080 \times 1400 au at 4 kpc. As our observations included only the ALMA 12 m array, the maximum recoverable scale is 4.2 arcsec \sim 16 800 au (at 4 kpc).

Table 2. Observing and image cube parameters for narrow spectral windows.

Telescope	Targeted line	Line Rest Frequency ^a (GHz)	E_u/k_B^a (K)	Bandwidth (MHz)	Δv^b (kHz)	Δv^c (km s ⁻¹)	Synthesized beam arcsec × arcsec [°]	rms noise ^d (mJy beam ⁻¹) (K)	
ALMA	N ₂ H ⁺ (3–2)	279.5117491	26.8	468.75	122.07	0.5	0.57 × 0.41 [83.2]	6.1	0.41
ALMA	DCN (4–3)	289.644917	34.8	117.1875	122.07	0.5	0.55 × 0.40 [82.0]	6.3	0.42
ALMA	³⁴ SO 6 ₇ –5 ₆	290.562238	63.8	117.1875	122.07	0.5	0.55 × 0.40 [82.2]	6.0	0.39
ALMA	H ₂ CO 4 _{0,4} – 3 _{0,3}	290.623405	34.9	117.1875	122.07	0.5	0.55 × 0.40 [82.3]	6.0	0.39
ALMA	C ³³ S (6–5)	291.485935	49.0	117.1875	122.07	0.5	0.55 × 0.40 [82.4]
VLA	NH ₃ (1,1)	23.694496	24.4	8.0	15.625	0.4	0.56 × 0.54 [28.0]	1.24	8.93
VLA	NH ₃ (2,2)	23.722631	65.6	8.0	15.625	0.4	0.56 × 0.54 [28.5]	1.18	8.47
VLA	NH ₃ (3,3)	23.870130	124.7	8.0	15.625	0.4	0.56 × 0.54 [30.5]	1.13	8.01
VLA	NH ₃ (5,5)	24.532985	296.5	8.0	15.625	0.4	0.55 × 0.54 [38.4]	1.10	7.52
VLA	NH ₃ (6,6)	25.056025	409.2	4.0	15.625	0.4	0.55 × 0.54 [41.1]	0.95	6.23
VLA	NH ₃ (7,7)	25.715182	539.7	4.0	15.625	0.4	0.54 × 0.53 [47.8]	1.06	6.84
VLA ^e	CH ₃ OH 3(2,1)–3(1,2)	24.928707	36.2	2.0	15.625	0.4	0.56 × 0.55 [31.5]	1.04	6.76
VLA ^e	CH ₃ OH 5(2,3)–5(1,4)	24.9590789	57.1	2.0	15.625	0.4	0.55 × 0.54 [49.7]	1.01	6.67
VLA ^e	CH ₃ OH 8(2,6)–8(1,7)	25.2944165	105.8	2.0	15.625	0.4	0.57 × 0.55 [52.8]	0.85	5.18
VLA ^e	CH ₃ OH 10(2,8)–10(1,9)	25.8782661	150.0	2.0	15.625	0.4	0.56 × 0.54 [65.0]	1.19	7.18

^a From CDMS (Müller et al. 2001, 2005) for lines observed with ALMA and from the TopModel line list for NH₃ lines, both accessed via the NRAO spectral line catalogue (Splatalogue; <https://splatalogue.online/>). CH₃OH line frequencies are from Müller, Menten & Mäder (2004).

^b Channel spacing. For the ALMA data, the Hanning-smoothed spectral resolution is 0.244 MHz for all of the narrow spws.

^c Velocity channel width of image cubes; see Sections 2.1 and 2.2.

^d Median rms noise estimated from emission-free channels; the rms noise is up to ~1.5 times higher in channels with bright and/or complex emission. The conversion to brightness temperature assumes the Rayleigh-Jeans approximation: $T = 1.222 \times 10^3 \frac{I}{v^2 \theta_{\text{maj}} \theta_{\text{min}}}$, where I is the rms in mJy beam⁻¹, v is the frequency in GHz, and $\theta_{\text{maj}} \times \theta_{\text{min}}$ is the synthesized beam size in arcseconds.

^e As in Towner et al. (2017), these 25 GHz CH₃OH lines will be referred to in the main text by the following shorthand notation, given by the first two values of the upper state quantum number of each transition respectively: 3₂, 5₂, 8₂, and 10₂.

After applying the solutions from the continuum self-calibration, the continuum-subtracted line data were imaged with Briggs weighting with a robust parameter of 0.5. For the narrow spws, which were imaged with 0.5 km s⁻¹ channels for better sensitivity to faint emission, the synthesized beamsizes and rms noise levels of the image cubes are listed in Table 2. For the wide spws, which were imaged with the native channel spacing, the synthesized beamsizes are 0′.60 × 0′.43 [P.A. 79.8°] and 0′.57 × 0′.41 [P.A. 78.9°] for the spws centred at ~278.2 and ~292.0 GHz, respectively, and the rms noise is ~3 mJy beam⁻¹ in emission-free channels (in channels with complex emission, the rms is up to ~1.5 times higher; see also Paper I). All measurements were made from images corrected for the response of the primary beam.

2.2 Karl G. Jansky Very Large Array

In this paper, we present our K-band VLA spectral line observations of G19.01–0.03. Our VLA tuning included 10 narrow spws targeting NH₃ and CH₃OH lines observed in other EGOs, including lines that exhibit maser activity in some EGOs (e.g. Brogan et al. 2011; Towner et al. 2017, see also Sections 3.2.3 and 3.2.4). The VLA observing parameters are summarized in Table 1 and details of the narrow spws are given in Table 2. The VLA K-band tuning also included 16 × 0.128 GHz spws for continuum, as detailed in Paper I, which presented the continuum results; for completeness, key parameters of the VLA 1.21 cm continuum image are included in Table 1.

As explained in Paper I, the VLA data were calibrated using the CASA 4.7.1 version of the VLA calibration pipeline. The data were Hanning smoothed, and phase-only self-calibration was performed using the channel with the strongest NH₃(3,3) emission (after continuum subtraction in the u, v -plane). These solutions were then applied to all of the line data (as well as to the continuum; see Paper I). For each narrowband spw, continuum subtraction was performed in the u, v -plane and the continuum-subtracted line data were

imaged with 0.4 km s⁻¹ channels, Briggs weighting with a robust parameter of 0.5, and a uv taper of 200 kλ to improve the brightness temperature sensitivity. The synthesized beamsizes and rms noise levels of the resulting image cubes are presented in Table 2. Measurements were made from images corrected for the primary beam response.

3 RESULTS

3.1 ALMA 1.05 mm continuum emission

In Paper I, we presented the ALMA 1.05 mm continuum towards MM1, and noted the detection of a further four continuum sources in the field for the first time (see Fig. 2), named MM2...MM5 in order of decreasing peak intensity. Their observed properties (as well as the observed properties of MM1 as presented in Paper I) are listed in Table 3, with their full-width at half maximum (FWHM) extents represented by pink ellipses in Fig. 2b. As detailed in Paper I, sources were extracted using the ASTRODENDRO algorithm (Rosolowsky et al. 2008), with a minimum isocontour value (I_{min}) of $5\sigma_{\text{rms}}$ (where $\sigma_{\text{rms}} = 0.25$ mJy beam⁻¹), minimum isocontour spacing (ΔI_{min}) of $1\sigma_{\text{rms}}$, and minimum size of a structure (n_{pix}) of $\approx n_{\text{pix, beam}}/2$ (i.e. half the beam size, where $n_{\text{pix, beam}} \approx 50$). Two sources to the south-west of MM4 are detected with peak emission $>5\sigma_{\text{rms}}$ (Fig. 2) but are only extracted by the dendrogram algorithm if the parameters are dropped to $\Delta I_{\text{min}} = 0.9\sigma_{\text{rms}}$ and $n_{\text{pix}} = 15$ pixels, meaning that they are only equivalent to a third of a beam in size. We therefore do not consider these firm detections. MM2...MM5 have angular separations from MM1 of 1.6, 5.5, 6.1, and 2.6 arcsec, respectively, ranging between 0.03 and 0.12 pc at the 4 kpc distance, marking the first detection of other millimetre sources within the parent clump of MM1. MM4 appears non-Gaussian in its emission morphology, whilst MM2 lies within a common contour to MM1 with lower surface-brightness emission connecting the two sources. This

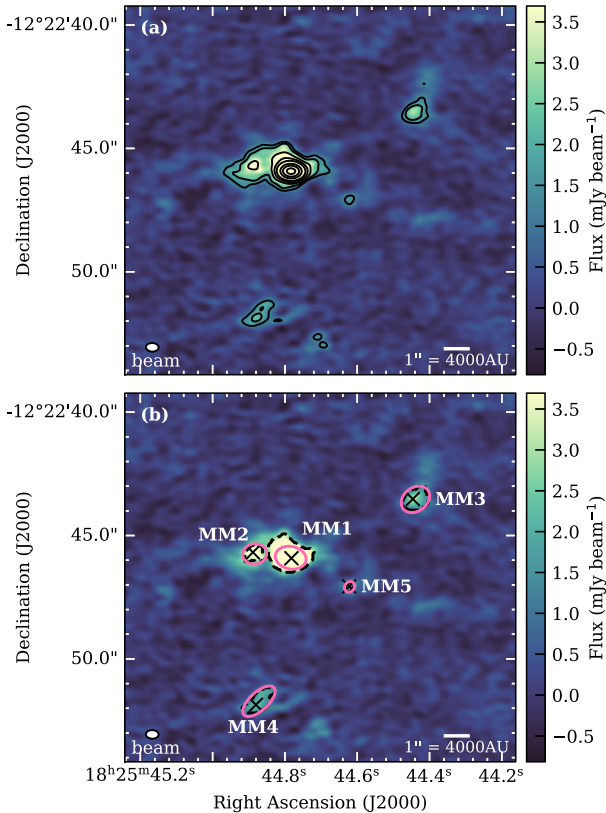


Figure 2. (a) ALMA 1.05 mm continuum image, corrected for the primary beam response, as shown in Paper I. The field shown is a sub-region of that mosaiced, which contains all emission detected $\geq 5\sigma$. Black contours are plotted at $[5, 8, 16, 32, 64, 200, 400, \text{and } 800] \times \sigma$, where $\sigma = 0.25 \text{ mJy beam}^{-1}$. The synthesized beam and scalebar are plotted in the bottom left and bottom right, respectively. (b) Same as (a), but with the outlines of the extracted dendrogram structures in dashed black, and ellipses representing the source sizes (Table 3) in pink. The peak positions of the sources (Table 3) are marked by the black \times s.

suggests that MM2 may be fragmenting out of material that also feeds MM1.

3.2 Line emission

3.2.1 COMs towards MM1 with ALMA

A forest of molecular lines is observed towards MM1 with ALMA, as seen in the wideband spectra shown here in Fig. 3. We follow the criteria presented by Herbst & van Dishoeck (2009) in identifying molecular lines (also see Maret et al. 2011). As outlined in Paper I, we attribute peaks in emission to cataloged rest frequencies from the JPL (Pickett et al. 1998) and CDMS (Müller et al. 2001) data bases at the source systemic velocity ($59.9 \pm 1.1 \text{ km s}^{-1}$; Cyganowski et al. 2011a). We further produced local thermodynamic equilibrium (LTE) synthetic spectra of the molecular emission (using the WEEDS extension of CLASS; Maret et al. 2011) – a molecular transition was positively identified when all lines for that species predicted in the synthetic spectrum were present in the observed spectrum, for typical model parameters expected of a hot core (e.g. $T > 100 \text{ K}$). The use of LTE synthetic spectra also allowed the identification of some emission peaks that were consistent with multiple line rest

frequencies within our spectral resolution ($\sim 1 \text{ km s}^{-1}$ in the wide spws), for example blended lines and lines with shoulder features. Using this approach, we identify 43 line transitions from 11 different species in the wide ALMA spws at ~ 278 and $\sim 292 \text{ GHz}$ (see Fig. 3 and Table 4), including isolated lines, blended lines, and lines with shoulder features. We note that many lines remain unidentified despite their strong detection above the noise, generally due to rest frequencies and/or synthetic line profiles that cannot be confidently distinguished at our spectral resolution. Of particular note, we report compact emission towards MM1 (see fig. 3 of Paper I) from a range of COMs, including Oxygen and Nitrogen-bearing COMs such as CH_3OCH_3 , CH_3CHO , CH_3OH , NH_2CHO , and CH_3OCHO . We also include in our analysis of MM1’s line emission (Sections 4.1 and 4.3) additional lines from three of these species that are serendipitously included in the narrow, targeted ALMA bands: CH_3OCHO ($27_{1,27} - 26_{0,26}$) with $\nu_{\text{rest}} = 289.62659 \text{ GHz}$ and $E_u/k_B = 385.4 \text{ K}$ (blended with the $\text{CH}_3\text{OH}(6_{1,2} - 5_{1,2})$ line with $\nu_{\text{rest}} = 289.62430 \text{ GHz}$ and $E_u/k_B = 731.4 \text{ K}$), CH_3OH ($11_{2,10} - 10_{3,7}$) with $\nu_{\text{rest}} = 279.35193 \text{ GHz}$ and $E_u/k_B = 190.9 \text{ K}$, and OCS ($23 - 22$) with $\nu_{\text{rest}} = 279.6853 \text{ GHz}$ and $E_u/k_B = 161.1 \text{ K}$. The majority of the lines targeted with narrow spws (Section 2.1 and Table 2) exhibit extended emission and are discussed in Section 3.2.2. The exception is $^{34}\text{SO } 6_7 - 5_6$, which exhibits compact emission but which we do not include in our analyses due to line blending in the narrowband cube.

In contrast, in the SMA data presented by Cyganowski et al. (2011a), MM1 was relatively line-poor (see Section 1): the only detected COM emission in their 2 GHz-wide bands, centred at ~ 220 and $\sim 230 \text{ GHz}$, was from CH_3OH and CH_3CN . With ALMA, we also detect molecular lines with up to four times higher E_u/k_B than detected with the SMA (e.g. $\text{CH}_3\text{OH}(23_{4,19} - 22_{5,18})$ at $E_u/k_B = 736 \text{ K}$), and identify 19 lines with $E_u/k_B > 200 \text{ K}$. The relative dearth of molecular lines in the SMA spectra is likely attributable to a combination of sensitivity and beam dilution; our ~ 0.4 arcsec-resolution ALMA observations improve on the 2.4 arcsec-resolution SMA observations by a factor of ~ 30 in beam area, and a factor of ~ 1.8 in brightness temperature sensitivity. Comparing our ALMA detections with those from the sensitive, 29 arcsec-resolution 1 mm single-dish survey of He, Takahashi & Chen (2012) confirms the importance of beam dilution: their observations of G19.01–0.03 have a 1σ rms of $0.015 - 0.022 \text{ K}$ (compared to 0.25 and 0.44 K for the ALMA and SMA observations, respectively), but the only COM detected is CH_3OH . In sum, our ALMA results affirm the hot core classification of G19.01–0.03 MM1 and illustrate the importance of sensitive, high-resolution observations for studying the chemistry of MYSOs.

3.2.2 Extended emission with ALMA

Fig. 4 presents peak intensity maps of a selection of lines that are representative of the extended emission in our ALMA tuning. These include three of the lines targeted in our narrow spectral windows ($\text{N}_2\text{H}^+(3-2)$, $\text{DCN } v = 0 (4 - 3)$ and $\text{H}_2\text{CO}(4_{0,4} - 3_{0,3})$, with $E_u/k_B = 26.8, 34.8,$ and 34.9 K , respectively), and three from our wide spectral windows ($\text{H}_2\text{CO}(4_{2,3} - 3_{2,1})$, $\text{CH}_3\text{OH}(6_{1,5} - 5_{1,4})$ and $\text{CH}_3\text{OH}(9_{-1,9} - 8_{0,8})$, with $E_u/k_B = 82.1, 63.7,$ and 110.0 K respectively). The $\text{H}_2\text{CO}(4_{2,3} - 3_{2,1})$ and $\text{CH}_3\text{OH}(6_{1,5} - 5_{1,4})$ lines in Figs 4(c) and (d) were identified as having extended emission around MM1 in Paper I.

Table 3. Observed properties of extracted 1.05 mm continuum sources.

Source	J2000.0 Coordinates ^a		Peak intensity ^b (mJy beam ⁻¹)	Integ. flux ^b (mJy)	Source size ^c Maj. × Min. (P.A.) (arcsec × arcsec [°])	Source size ^c (AU)
	α (^h ^m ^s)	δ ([°] ['] ^{''})				
MM1	18:25:44.782	−12:22:45.92	266.3	303.1	1.15 × 0.84 [78.7]	4600 × 3360
MM2	18:25:44.888	−12:22:45.68	4.7	8.1	0.83 × 0.74 [− 82.1]	3310 × 2970
MM3	18:25:44.446	−12:22:43.52	3.0	7.1	1.14 × 0.88 [− 53.0]	4560 × 3530
MM4	18:25:44.880	−12:22:51.86	2.3	6.0	1.56 × 0.65 [− 47.7]	6200 × 2610
MM5	18:25:44.622	−12:22:47.06	1.6	–	–	–

^a Peak position. The number of significant figures reflects a one-pixel uncertainty.

^b Evaluated within the intensity-weighted second moment size (not the total dendrogram structure). For sources smaller than a beam, integrated fluxes are marked ‘–’.

^c Deconvolved major and minor axes sizes; position angle is measured East of North, i.e. positive in the anti-clockwise direction. Sizes are the intensity-weighted second moment, converted to FWHM (see Paper I). Sources smaller than a beam are marked ‘–’.

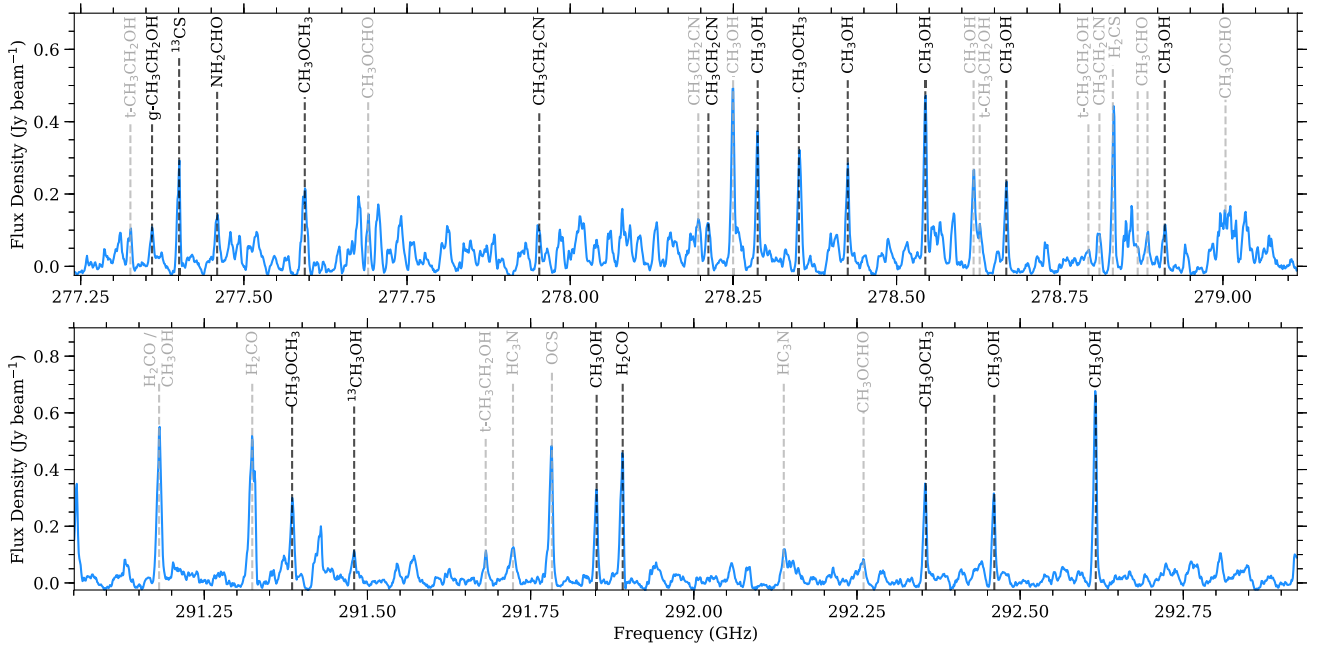


Figure 3. ALMA spectra towards the 1.05 mm continuum peak of MM1 in the broad spectral windows centred at 278.209 and 292.021 GHz. Unlabelled lines could not be confidently identified, mostly due to blending at the coarse spectral resolution of our observations. Lines labelled in black were used for the kinematic analysis presented in Paper I, while others are labelled in grey. All marked lines are listed in Table 4.

The four H₂CO and CH₃OH lines shown in Fig. 4 appear to spatially trace the same bi-polar outflow structure identified by Cyganowski et al. (2011a) in ¹²CO(2–1) with the SMA (see Fig. 1) and in HCO⁺(1–0) and SiO(2–1) with CARMA. Kinematically, however, the ALMA H₂CO and CH₃OH emission traces lower velocity gas than the SMA ¹²CO or the CARMA HCO⁺ emission, with a median full velocity extent of 25 km s⁻¹ compared to ~135 km s⁻¹ for ¹²CO(2–1) and ~76 km s⁻¹ for HCO⁺(1–0) (Cyganowski et al. 2011a). The H₂CO and CH₃OH kinematics seen with ALMA do however exhibit a similar asymmetry as observed with the SMA and CARMA, with the blue-shifted lobe extending to higher velocities (up to ~20 km s⁻¹ from the systemic velocity, V_{sys}) than the red-shifted lobe (up to ~9 km s⁻¹ from V_{sys}). Overplotted in Fig. 4(e) are the positions of 44 GHz Class I CH₃OH masers from Cyganowski et al. (2009), which appear to trace the outer edge of the CH₃OH and H₂CO outflow lobes. Taken together, our results are consistent with the ALMA CH₃OH and H₂CO emission tracing lower velocity, outflow–cloud interaction regions or outflow cavity

walls, as also seen in the EGO G11.92–0.61 by Cyganowski et al. (2017).

The CH₃OH(9_{-1,9} – 8_{0,8}) line in Fig. 4(e) (with v_{rest} = 278.30451 GHz) is known to exhibit Class I maser emission towards other sources in the literature (e.g. Voronkov et al. 2012; Yanagida et al. 2014; Cyganowski et al. 2017). Comparing the emission of this line with that of CH₃OH(6_{1,5} – 5_{1,4}) (v_{rest} = 292.67291 GHz), shown in Fig. 4(d), the two lines have similar emission morphologies. As shown in Fig. 5, these lines also have similar fluxes towards the ALMA 1.05 mm continuum peak of MM1 (equivalent to brightness temperatures of T_b = 39 and 33 K, respectively). However, towards the region of brightest CH₃OH(9_{-1,9} – 8_{0,8}) emission in the outflow (T_b = 49 K at 18^h25^m44^s.517 – 12[°]22′32″.652 (J2000)), the CH₃OH(6_{1,5} – 5_{1,4}) line is an order-of-magnitude weaker (Fig. 5) with T_b = 4 K. The CH₃OH(9_{-1,9} – 8_{0,8}) line is also notably narrower at the outflow position than towards the MM1 continuum peak (ΔV_{FWHM} = 2.01 ± 0.01 km s⁻¹ and 6.95 ± 0.08 km s⁻¹, respectively) and is spatially and kinematically coincident with

Table 4. Properties of spectral lines identified in the broad ALMA spectral windows towards MM1, arranged by decreasing E_u/k_B .

Species ^a	Transition	Frequency (GHz)	E_u/k_B (K)	$S_{ij}\mu^2$ (D ²)	g_u	Catalogue ^b	Paper I ^c
CH₃OH ($v_t = 0$)	23 _{4, 19} –22 _{5, 18}	278.96513	736.0	7.05321	47	JPL	Y
CH₃OH ($v_t = 0$)	21 _{-2, 20} –20 _{-3, 18}	278.47989	563.2	6.45393	43	JPL	Y
HC ₃ N ($v_7 = 1$)	J = 32–31, I = 1f	292.19837	551.4	443.01616	65	CDMS	N
HC ₃ N ($v_7 = 1$)	J = 32–31, I = 1e	291.78201	551.1	442.99035	65	CDMS	N
CH ₃ OH ($v_t = 0$)	17 _{6, 12} –18 _{4, 13} - -	291.90814	548.6	3.98258	35	JPL	Y
CH₃OH ($v_t = 0$)	18 _{5, 13} –19 _{4, 16} - -	278.72314	534.6	5.26251	37	JPL	Y
CH₃OH ($v_t = 0$)	18 _{5, 14} –19 _{4, 15} + +	278.67303	534.6	5.26201	37	JPL	N
CH ₃ OH ($v_t = 1$)	10 _{1, 10} –9 _{0, 9}	292.51744	418.8	5.01720	21	JPL	Y
CH ₃ OCHO ($v = 1$)	23 _{4, 19} –22 _{4, 18} A	292.31711	365.4	59.03484	94	JPL	N
t-CH ₃ CH ₂ OH	27 _{6, 22} –27 _{5, 23}	278.84892	363.7	28.22445	55	JPL	N
CH₃OH ($v_t = 0$)	14 _{4, 10} –15 _{3, 12}	278.59908	339.6	4.14979	29	JPL	Y
CH ₃ OH ($v_t = 0$)	15 _{1, 0} –14 _{2, 0}	291.24057	295.3	5.70014	31	JPL	N
t-CH ₃ CH ₂ OH	23 _{6, 17} –23 _{5, 18}	278.68234	277.5	23.74792	47	JPL	N
CH ₃ CH ₂ CN ($v = 0$)	31 _{7, 24} –30 _{7, 23}	278.00758	267.8	435.64965	63	JPL	Y
CH ₃ CH ₂ CN ($v = 0$)	31 _{6, 25} –30 _{6, 24}	278.26670	253.4	441.91785	63	JPL	Y
CH ₃ CH ₂ CN ($v = 0$)	31 _{6, 26} –30 _{6, 25}	278.25123	253.4	441.86236	63	JPL	N
CH ₃ CH ₂ CN ($v = 0$)	31 _{5, 26} –30 _{5, 25}	278.86581	241.4	447.13304	63	JPL	N
g-CH ₃ CH ₂ OH	16 _{6, 10} –15 _{6, 9} ($v_t = 0-0$)	277.41431	213.8	21.96640	33	JPL	Y
g-CH ₃ CH ₂ OH	16 _{4, 12} –15 _{4, 11} ($v_t = 0-0$)	278.64299	189.7	23.96604	33	JPL	Y
CH ₃ OCHO ($v = 0$)	24 _{2, 22} –23 _{2, 21} E	279.05752	178.5	62.00988	98	JPL	N
CH ₃ OCHO ($v = 0$)	24 _{2, 22} –23 _{2, 21} A	279.06596	178.5	62.01870	98	JPL	N
OCS ($v = 0$)	J = 24–23	291.83965	175.1	12.27714	49	CDMS	N
CH ₃ OCHO ($v = 0$)	22 _{6, 16} –21 _{6, 15} E	279.05067	175.0	54.25478	90	JPL	N
CH ₃ OCHO ($v = 0$)	22 _{6, 16} –21 _{6, 15} A	279.07471	175.0	54.26998	90	JPL	N
CH ₃ OCHO ($v = 0$)	23 _{4, 20} –22 _{4, 19} A	277.74543	173.4	58.74803	94	JPL	N
H ₂ CO	4 _{3, 2} –3 _{3, 1}	291.38049	140.9	28.54373	27	CDMS	N
t-CH ₃ CH ₂ OH	17 _{1, 16} –16 _{2, 15}	277.38114	131.5	7.54333	35	JPL	N
CH ₃ OCH ₃	16 _{1, 16} –15 _{0, 15} (EA)	292.41225	120.3	70.75903	66	JPL	Y
NH ₂ CHO	13 _{3, 10} –12 _{3, 9}	277.51403	119.8	482.76031	81	JPL	Y
CH ₃ OH ($v_t = 0$) ^d	9 _{-1, 9} –8 _{0, 8}	278.30451	110.0	5.82054	19	JPL	N
CH ₃ CHO ($v_t = 0$)	15 _{-1, 15} –14 _{-1, 14} (E)	278.92443	109.8	188.77851	62	JPL	N
CH ₃ CHO ($v_t = 0$)	15 _{1, 15} –14 _{1, 14} (A)	278.93944	109.7	188.63110	62	JPL	N
CH ₃ OCH ₃	13 _{2, 12} –12 _{1, 11} (EE)	291.44307	88.0	116.69078	216	JPL	Y
H ₂ CO ^d	4 _{2, 2} –3 _{2, 1}	291.94807	82.1	16.31005	9	CDMS	Y
H ₂ CO	4 _{2, 3} –3 _{2, 2}	291.23777	82.1	16.30879	9	CDMS	N
CH ₃ OCH ₃	12 _{2, 11} –11 _{1, 10} (EE)	278.40706	76.3	103.86585	200	JPL	Y
H ₂ CS ^d	8 _{1, 7} –7 _{1, 6}	278.88640	73.4	64.08219	51	JPL	N
CH ₃ OH ($v_t = 0$) ^d	6 _{1, 5} –5 _{1, 4} - -	292.67291	63.7	4.72131	13	JPL	Y
¹³ CH ₃ OH ($v_t = 0$)	3 _{2, 2} –4 _{1, 3}	291.53662	51.4	0.69489	7	CDMS	Y
t-CH ₃ CH ₂ OH	9 _{3, 6} –8 _{2, 7}	291.73815	49.2	7.83704	19	JPL	N
¹³ CS ($v = 0$)	6–5	277.45540	46.6	46.00530	26	CDMS	Y
CH ₃ OCH ₃	7 _{3, 5} –6 _{2, 4} (EE)	277.64832	38.1	65.30773	120	JPL	N
CH₃OH ($v_t = 0$)	2 _{-2, 1} –1 _{-3, -1, 3}	278.34222	32.9	0.32917	5	JPL	Y

^a Bold typeface indicates the lines used for the analysis presented in Sections 4.1.2–4.1.4.^b CDMS (Müller et al. 2001) and JPL (Pickett et al. 1998), accessed via the NRAO spectral line catalogue (Splatalogue; <https://splatalogue.online/>).^c Lines used for the kinematic analysis in Paper I are marked with a ‘Y’. Lines that are newly presented here are marked with an ‘N’.^d Outflow tracing, see Section 3.2.2.

44 GHz Class I CH₃OH masers (Cyganowski et al. 2009), candidate 229.759 GHz CH₃OH maser emission (Cyganowski et al. 2011a, see their fig. 12), and NH₃(3,3) masers (see Section 3.2.3). The coincidence with probable 229.759 GHz maser emission is notable because the 229.759 and 278.305 GHz transitions are in the same Class I maser series (the 36 GHz maser series; Voronkov et al. 2012), and Cyganowski et al. (2018) found that all 229 GHz masers in the EGO G11.92–0.61 have probable 278 GHz maser counterparts. Though the angular resolution of our ALMA observations is insufficient to rely on line brightness temperatures to distinguish between thermal and maser behaviour (as was also the case for G11.92–0.61 in Cyganowski et al. 2017), the line properties shown in Fig. 5, and the coincidence of the brightest CH₃OH(9_{-1, 9} – 8_{0, 8}) emission

in the outflow with other shock-excited masers, strongly suggest thermalized emission towards the MM1 hot core, and 278 GHz Class I CH₃OH maser emission tracing outflow–cloud interaction regions (e.g. Voronkov et al. 2012; Yanagida et al. 2014; Cyganowski et al. 2017). Higher angular resolution observations of the CH₃OH(9_{-1, 9} – 8_{0, 8}) line would be required to confirm the presence of maser emission based on brightness temperature.

As a dense gas tracer, N₂H⁺ is known to trace infrared-dark clumps at both quiescent and active evolutionary stages: Sanhueza et al. (2012), for example, detect N₂H⁺(1–0) towards the majority of their 92 infrared-dark clumps with the Mopra telescope at 38 arcsec angular resolution (typically ~0.8 pc across their sample). Notably, while we observe extended N₂H⁺(3–2) emission in G19.01–0.03

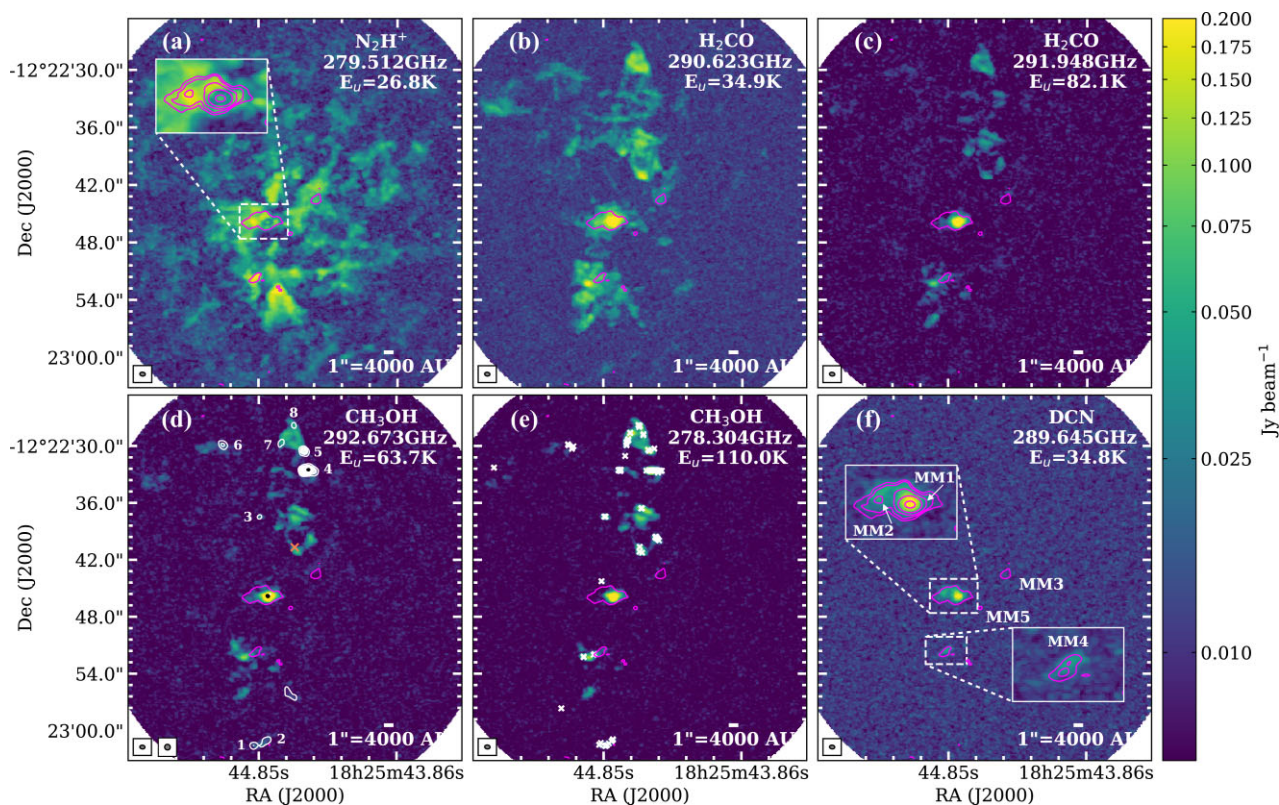


Figure 4. ALMA peak intensity maps of (a) $\text{N}_2\text{H}^+(3-2)$, (b) $\text{H}_2\text{CO}(4_{0,4}-3_{0,3})$, (c) $\text{H}_2\text{CO}(4_{2,3}-3_{2,1})$, (d) $\text{CH}_3\text{OH } \nu_r = 0(6_{1,5}-5_{1,4})$, (e) $\text{CH}_3\text{OH } \nu_r = 0(9_{-1,9}-8_{0,8})$, and (f) $\text{DCN } \nu = 0(4-3)$, in units of Jy beam^{-1} shown on a logarithmic scale (images shown are not primary beam corrected). Millimetre sources are labelled in (f), where two zoomed insets are also shown centred on MM1/MM2 and MM4. A zoomed inset of MM1/MM2 is also shown in (a). Overplotted magenta contours in all panels show the 1.05 mm continuum emission at 5σ . These contours are also shown in the zoomed insets, but at 5σ , 8σ , 16σ , 64σ , and 600σ (where $\sigma = 0.25 \text{ mJy beam}^{-1}$). In panel (d), white contours show the VLA $\text{NH}_3(3,3)$ peak intensity map (in 10 σ steps from 5 to 145 σ , where $\sigma = 1.1 \text{ mJy beam}^{-1}$, non-primary beam corrected), black contours show the VLA $\text{NH}_3(6,6)$ peak intensity map (at the 5σ level, where $\sigma = 0.9 \text{ mJy beam}^{-1}$, non-primary beam corrected), and the orange cross indicates the peak position of the candidate VLA 25 GHz $\text{CH}_3\text{OH } 5(2,3)-5(1,4)$ maser emission (see Section 3.2.4). The $\text{NH}_3(3,3)$ maser groups from Section 3.2.3 are numbered in panel (d) as in Table 5. Overplotted white crosses in (e) mark the positions of 44 GHz Class I CH_3OH masers from Cyganowski et al. (2009). Each panel shows the ALMA synthesized beam in the bottom left (as well as the VLA synthesized beam in panel (d)), a 1 arcsec scale bar in the bottom right, and the molecule name, frequency and upper energy in the top right.

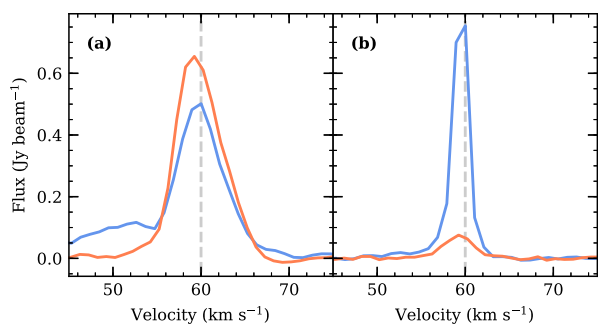


Figure 5. Spectra of the $\text{CH}_3\text{OH}(9_{-1,9}-8_{0,8})$ line at $E_u/k_B = 110.0 \text{ K}$ (in blue) and the $\text{CH}_3\text{OH}(6_{1,5}-5_{1,4})$ line at $E_u/k_B = 63.7 \text{ K}$ (in orange) towards (a) the ALMA 1.05 mm continuum peak of MM1 (Table 3), and (b) the position of peak $\text{CH}_3\text{OH}(9_{-1,9}-8_{0,8})$ emission in the northern outflow lobe (Section 3.2.2). The systemic velocity of MM1 ($59.9 \pm 1.1 \text{ km s}^{-1}$; Cyganowski et al. 2011a) is marked by the vertical dashed line.

(Fig. 4a), its morphology does not resemble that of the 1.05 mm dust emission or that of the outflow structure. Cyganowski et al. (2017) found similar results in their ALMA $\text{N}_2\text{H}^+(3-2)$ observations of the EGO G11.92–0.61 (their fig. 3c), suggesting that in high-mass

clumps the $\text{N}_2\text{H}^+(3-2)$ and millimetre continuum emission do not trace the same structures on small size scales.¹ We also note that larger-scale $\text{N}_2\text{H}^+(3-2)$ emission will be affected by spatial filtering due to missing short-spacing information (Table 1; Section 2.1). The morphology of the $\text{DCN}(4-3)$ emission, on the other hand (Fig. 4f), more closely resembles the ALMA 1.05 mm continuum. $\text{DCN}(4-3)$ is detected towards MM1 to 38σ (where $\sigma = 6.3 \text{ mJy beam}^{-1}$); the position of the DCN emission peak is offset from the ALMA 1.05 mm continuum peak by 0.1 arcsec $\sim 400 \text{ au}$ (within a DCN beam; Table 2), likely due to line opacity and self-absorption towards the continuum peak. The DCN emission also traces some of the nearby millimetre companions to MM1, which is discussed in Section 3.2.5.

3.2.3 Ammonia emission with the VLA

Of the ammonia lines in our VLA tuning, $\text{NH}_3(3,3)$ and $\text{NH}_3(6,6)$ are known to exhibit maser behaviour thought to arise due to outflow-induced shocks (e.g. Mangum & Wootten 1994; Kraemer & Jackson

¹ $\text{N}_2\text{H}^+(3-2)$ is detected in absorption against the millimetre continuum of MM1, see Appendix A.

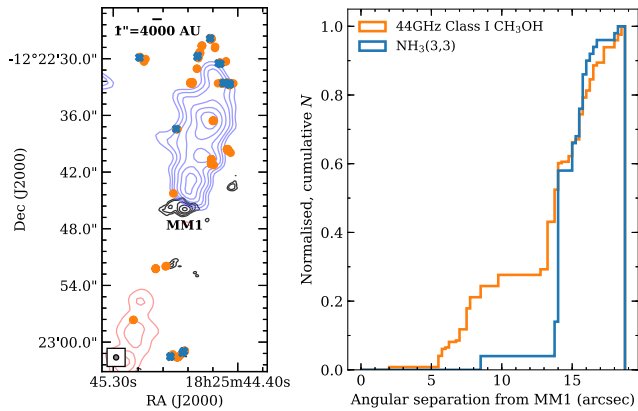


Figure 6. *Left-hand panel:* Fitted positions of each $\text{NH}_3(3,3)$ spot across all groups (blue \times), and 44 GHz Class I CH_3OH maser spot positions from Cyganowski et al. (2009; orange filled circles). ALMA 1.05 mm continuum contours are plotted in black (at [5, 8, 16, 64, and 600] $\times \sigma$, where $\sigma = 0.25 \text{ mJy beam}^{-1}$). High-velocity, blue- and red-shifted $^{12}\text{CO}(2-1)$ emission observed with the SMA (Cyganowski et al. 2011a) are plotted in blue and red contours, as in Fig. 1. The VLA beam and a scalebar are plotted in the bottom left and top left of the panel, respectively. *Right-hand panel:* Normalized, cumulative histogram of the angular separation (in arcsec) of each $\text{NH}_3(3,3)$ spot (blue), and each 44 GHz Class I CH_3OH maser spot (orange), from the ALMA 1.05 mm continuum peak of MM1 (Table 3). Angular separations were calculated using the `au.angularSeparation` task of the `ANALYSISUTILS` PYTHON package.

1995; Brogan et al. 2011). Towards G19.01–0.03, spatially compact regions of $\text{NH}_3(3,3)$ emission are detected at the $\geq 5\sigma$ level (shown as white contours in Fig. 4d) coincident both spatially and kinematically with the outflow-tracing ALMA H_2CO and CH_3OH emission shown in Figs 4(b)–(e). To characterize the $\text{NH}_3(3,3)$ emission, we identify as firm detections, and potential maser candidates, locations where $\geq 5\sigma$ emission in ≥ 2 consecutive velocity channels is spatially contiguous within a VLA beam. Following the terminology of Towner et al. (2021), we refer to emission in a single velocity channel (each 0.4 km s^{-1} wide; Table 2) as a ‘spot’, and emission from multiple spatially contiguous spots as a ‘group’: a group thus contains at least two spots.

To extract the position, peak intensity and velocity of each $\geq 5\sigma$ emission spot, we fit the observed emission with a 2D Gaussian using the `CASA IMFIT` task (as in Towner et al. 2021). The rms noise is measured in each channel to ascertain the signal to noise of the detection as the noise is higher in channels with bright emission due to dynamic range limitations. As we expect the emission to be unresolved, we fit each emission spot as a point source by fixing the size to that of the synthesized beam (e.g. Hunter et al. 2018; Towner et al. 2021). In total, we identify 50 emission spots at the $\geq 5\sigma$ level (where the mean σ across all channels with emission is $\sigma = 1.14 \text{ mJy beam}^{-1}$) that reside in eight emission groups. The position of each emission spot is plotted in Fig. 6, each maser group is labelled in Fig. 4(d), and Table 5 lists the properties of each group. Unlabelled contours in Fig. 4(d) correspond to emission that does not meet our criteria of $\geq 5\sigma$ emission in ≥ 2 consecutive velocity channels within a VLA beam (generally because the emission centroids shift by more than a beam in consecutive channels) and so is not included in our analysis. The strongest emission group (ID 4 in Table 5) has a fitted peak intensity ($216.0 \pm 1.3 \text{ mJy beam}^{-1}$) corresponding to a brightness temperature $\sim 1550 \text{ K}$, strongly suggestive of masing behaviour. Four additional emission groups (i.e. IDs 1, 2, 5, and 6) also exhibit brightness temperatures greater than the E_u/k_B of the

line. While the brightest group (ID 4) spans both blue- and red-shifted velocities (Table 5), blue-shifted and red-shifted $\text{NH}_3(3,3)$ emission groups generally reside towards the blue- and red-shifted outflow lobes, respectively. The same pattern was observed in 44 GHz Class I CH_3OH masers by Cyganowski et al. (2009; their fig. 5f), though the maser velocities are modest compared to the velocity extent of the thermal molecular outflow lobes (Cyganowski et al. 2009, 2011a). All $\text{NH}_3(3,3)$ emission spots are coincident both spatially and kinematically (within a beam and a channel, respectively) with 44 GHz Class I CH_3OH maser spots from Cyganowski et al. (2009; see fig. 6), similar to the results seen in the EGO G35.03+0.35 by Brogan et al. (2011). We note that in G19.01–0.03, not all 44 GHz methanol masers are coincident with $\text{NH}_3(3,3)$ masers.

In G19.01–0.03, all identified $\text{NH}_3(3,3)$ emission spots are located in the outer portions of the bipolar outflow lobes, while the 44 GHz Class I methanol maser spots are also found closer to the driving source. This distinction is shown in Fig. 6, which plots the normalized, cumulative distribution of the angular separation (θ_{sep}) of each $\text{NH}_3(3,3)$ and 44 GHz Class I CH_3OH maser spot from the ALMA 1.05 mm dust continuum peak of MM1. The two-sample Kolmogorov–Smirnov (K-S) and k -sample Anderson–Darling (A-D) tests are both non-parametric null hypothesis tests often used to compare two such distributions. The null hypothesis in this case states that the two distributions may be drawn from the same underlying distribution if the tests return p -values larger than 0.05. Running both the K-S and A-D tests on the full range of angular separations (θ_{sep}) shown in Fig. 6 returns vanishingly small p -values, meaning the null hypothesis may be rejected and a conclusion drawn that the $\text{NH}_3(3,3)$ and 44 GHz methanol maser distributions are significantly different. However, running both tests for $\theta_{\text{sep}} \geq 12.5 \text{ arcsec}$ returns $p \gg 0.05$, meaning that the two distributions at large angular separations are effectively indistinguishable and may be drawn from the same underlying distribution.

We note that thermal $\text{NH}_3(1,1)$ and $(2,2)$ emission are detected towards G19.01–0.03 at 73 arcsec-resolution by Cyganowski et al. (2013) but are undetected in our VLA observations (to 5σ limits of 6.2 and $5.9 \text{ mJy beam}^{-1}$, respectively). Our non-detection of these low- J transitions is primarily attributable to the limited brightness temperature sensitivity of our high-resolution observations (Table 2), with spatial filtering potentially contributing to the non-detection of the $\text{NH}_3(2,2)$ line (the maximum recoverable scale of our observations is only $\sim 4.5 \text{ arcsec} \sim 0.08 \text{ pc}$ at $D = 4 \text{ kpc}$, see Table 1). Cyganowski et al. (2013) also detect $\text{NH}_3(3,3)$ towards G19.01–0.03 that is likely dominated by thermal emission, presumably arising near MM1. Extended $\text{NH}_3(3,3)$ emission is also seen towards the mm continuum sources in the EGO G35.03+0.35 by Brogan et al. (2011) in $3.7 \times 3.0 \text{ arcsec}$ resolution VLA observations ($\sim 8, 580 \times 6960 \text{ au}$ at the parallax distance of $2.32^{+0.24}_{-0.20} \text{ kpc}$ from Wu et al. 2014). In our data, $\text{NH}_3(3,3)$ emission at $\geq 5 \times$ the median rms in Table 2 is present in a single channel within the area of MM1’s mm continuum emission. This channel, however, has bright maser emission and so an elevated rms, and the $\text{NH}_3(3,3)$ peak is $< 5 \times$ the channel rms. Since the $\text{NH}_3(3,3)$ peak is also offset from the mm continuum peak and our tentative $\text{NH}_3(6,6)$ and $(7,7)$ detections (see below), we conclude that $\text{NH}_3(3,3)$ is undetected towards MM1 in our data. $\text{NH}_3(5,5)$ is also undetected in our VLA observations, to a 5σ limit of $5.5 \text{ mJy beam}^{-1}$.

$\text{NH}_3(6,6)$ emission (shown in black contours in Fig. 4d) is detected at the 5.7σ level ($I_{\text{peak}} = 5.4 \text{ mJy beam}^{-1}$) towards a position in the outskirts of the northern, blue-shifted outflow lobe

Table 5. Properties of NH₃(3,3) emission groups.

Group ^a ID	α (hms)	J2000.0 centroid position ^b			I_{peak}^c (mJy beam ⁻¹)	Angular spread ^d α, δ (", ")	$V_{\text{min}}, V_{\text{max}}^e$ (km s ⁻¹)	V_{peak}^f (km s ⁻¹)
		dx (")	δ (° / ")	dy (")				
1	18:25:44.89	0.02	–12:23:01.55	0.02	20.1 (1.2)	0.012, 0.044	60.2, 61.4	60.6
2	18:25:44.79	0.02	–12:23:01.02	0.02	18.9 (1.3)	0.073, 0.091	59.8, 61.4	60.2
3	18:25:44.85	0.03	–12:22:37.44	0.03	9.5 (1.2)	0.016, 0.022	57.4, 57.8	57.4
4	18:25:44.49	0.01	–12:22:32.60	0.01	216.0 (1.3)	0.262, 0.059	51.4, 61.8	59.8
5	18:25:44.53	0.01	–12:22:30.54	0.01	59.0 (1.3)	0.092, 0.030	57.8, 59.4	59.0
6	18:25:45.11	0.02	–12:22:29.89	0.02	26.2 (1.3)	0.048, 0.019	59.0, 59.4	59.4
7	18:25:45.69	0.03	–12:22:29.73	0.03	12.4 (1.3)	0.039, 0.067	58.6, 59.4	59.4
8	18:25:44.60	0.03	–12:22:27.85	0.03	11.9 (1.3)	0.041, 0.037	59.4, 59.8	59.8

^a Labelled from south to north, see Fig. 4(d).

^b Intensity-weighted centroid position and intensity-weighted mean statistical error from the Gaussian fitting, of each emission group.

^c Fitted peak intensity of the brightest emission spot in each group (i.e. from a single channel). The statistical error from the Gaussian fitting is listed in parentheses. $T_B(\text{K}) \approx 7186 \times I(\text{Jy beam}^{-1})$.

^d The angular spread of the emission group, calculated as the standard deviation of the difference between the position of each individual emission spot (i.e. from a single channel) and the intensity-weighted centroid position of the group.

^e Velocity spread over which $\geq 5\sigma$ emission is present, see Section 3.2.3.

^f Velocity of the channel at which the brightest emission in each group appears.

(18^h25^m44^s.50 –12°22′32″.52 (J2000)), spatially and kinematically coincident with an NH₃(3,3) maser group (ID 4 in Table 5), 44 GHz Class I CH₃OH masers (Cyganowski et al. 2009), and candidate ALMA 278.3 GHz Class I CH₃OH maser emission (Section 3.2.2). Towards MM1, NH₃(6,6) is detected at the 5.6 σ level ($I_{\text{peak}} = 5.3$ mJy beam⁻¹), spatially and kinematically coincident with a tentative 4.4 σ (4.6 mJy beam⁻¹) detection of NH₃(7,7). These tentative high-J detections towards MM1 could represent tentative evidence of emission from hot gas originating in the inner regions of the circumstellar accretion disc around the central MYSO(s) (Paper I).

3.2.4 25 GHz methanol emission with the VLA

The four CH₃OH lines in our VLA tuning (Table 2) can exhibit thermal and/or Class I maser emission and are commonly detected towards EGOs: in their study of 20 EGOs, Towner et al. (2017) detected thermal and/or maser emission towards 16 (80 per cent) of their sources. As Towner et al. (2017) adopt a 4 σ detection criterion, we consider $\geq 4\sigma$ 25 GHz CH₃OH emission so that we can compare to their results; we also adopt their shorthand notation of 3₂, 5₂, 8₂, and 10₂ for these lines. Towards MM1, we tentatively detect all four lines at the 4.8, 5.5, 4.5, and 4.5 σ levels, respectively (see Fig. 7, and Table 2 for σ values), equivalent to brightness temperatures (T_B) of 32.6, 36.8, 23.2, and 32.4 K. Towner et al. (2017) detect all four 25 GHz CH₃OH lines in half of their sample (i.e. ~ 63 per cent of those with a detection of at least one line). The strongest emission towards MM1 is in the 5₂ line, a result also reported by Towner et al. (2017) towards the majority of the sources in their sample. We also detect 7.8 σ 5₂ emission ($T_B = 52.3$ K) offset by 6 arcsec $\sim 24,000$ au to the north-west of MM1 (see Figs 4d and 7). This 5₂ emission is positionally and kinematically coincident with outflow-tracing H₂CO and CH₃OH emission observed with ALMA (Section 3.2.2 and Fig. 4) and with 44 GHz Class I CH₃OH maser emission (Cyganowski et al. 2009).

To distinguish between thermal and maser 25 GHz CH₃OH emission, we consider the two approaches detailed by Towner et al. (2017): (i) following criteria on the spatial and spectral extent of the line emission, and (ii) comparing observed line intensities to predictions for optically thin LTE emission. For the first approach, spatially and spectrally broad emission (i.e. resolved

$\geq 4\sigma$ emission in ≥ 5 channels ~ 2 km s⁻¹) is considered thermal, while unresolved/point-like spectrally narrow emission (i.e. $\geq 4\sigma$ emission in ≤ 4 channels ~ 1.6 km s⁻¹) is considered a candidate maser. The strongest 5₂ emission towards the MM1 outflow appears both unresolved (i.e. with spatial extent less than a beam) and spectrally narrow with a fitted FWHM velocity width (ΔV_{FWHM}) of 0.6 ± 0.1 km s⁻¹. We therefore consider this a candidate maser. Towards MM1, the emission from all four 25 GHz CH₃OH lines appears spatially unresolved. Both broad and narrow Gaussian components are needed to describe the 5₂ emission towards MM1, with velocity widths of 3.5 ± 0.1 and 0.7 ± 0.1 km s⁻¹, respectively, while the spectral profiles of the 3₂, 8₂, and 10₂ lines are best fit by single Gaussians with velocity widths of 3.4 ± 0.1 , 6.0 ± 0.2 , and 6.7 ± 0.2 km s⁻¹, respectively. All of the fitted Gaussian components have centroid velocities consistent with the systemic velocity of MM1 (59.9 ± 1.1 km s⁻¹; Cyganowski et al. 2011a). The 8₂ and 10₂ lines also have velocity widths of a similar order to the thermal CH₃OH emission seen with ALMA towards MM1 (see left-hand panel of Fig. 5). Line models under LTE and optically thin conditions (produced using the WEEDS package of the CLASS software) reasonably describe the broad emission components of all four lines towards MM1. As a whole, our data suggest that both thermal (broad components) and weak maser (narrow 5₂ component) may be present towards MM1, though we emphasize that this is a tentative result due to the low S/N of the 25 GHz CH₃OH emission towards MM1.

3.2.5 MM2...MM5 with ALMA and the VLA

In Fig. 8, we show spectra for the broad ALMA spectral windows towards the 1.05 mm continuum peaks of MM2, MM3, MM4, and MM5. The lines shown in Figs 4(c)–(e) lie within these broad-bands. MM3 and MM5 appear devoid of molecular line emission in these bands, while MM2 and MM4 both have $> 5\sigma$ detections of a handful of lines (labelled in Fig. 8). All of the line emission detected towards MM2 and MM4 in these broad-bands appears spatially and kinematically coincident with emission attributed to the outflow driven by MM1 (including the H₂CO and CH₃OH lines shown in Figs 4c–e; see Section 3.2.2). As such, it is likely that this line emission is associated with the MM1 outflow, rather than being physically associated with MM2 and MM4. N₂H⁺(3–2) emission (see Fig.

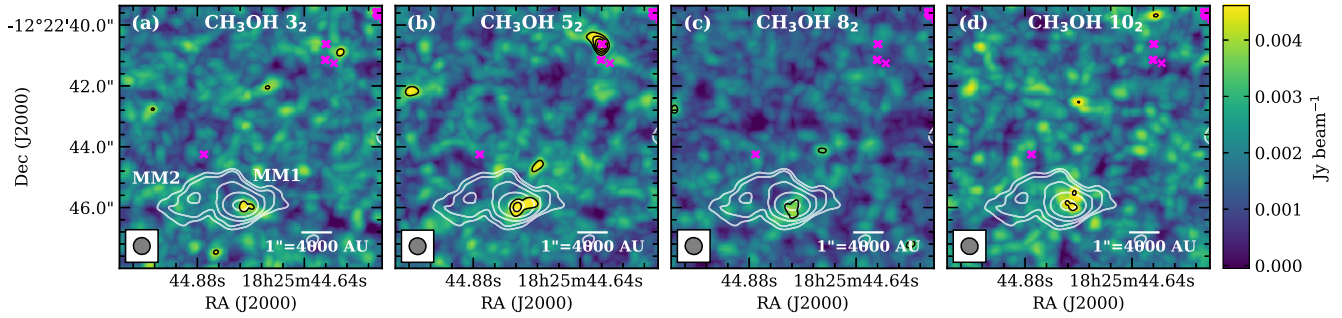


Figure 7. VLA peak intensity maps of the four ~ 25 GHz CH_3OH lines in our VLA tuning (Table 2), here referred to by the short hand notation 3_2 , 5_2 , 8_2 , and 10_2 . Each panel shows the peak intensity map of the labeled transition in colourscale and black contours, with contour levels of 4σ for the 3_2 , 8_2 , and 10_2 lines (where $\sigma = 1.04$, 0.85 , and 1.19 mJy beam $^{-1}$, respectively), and $[4, 5, 6, \text{ and } 7] \times \sigma$ for the 5_2 line (where $\sigma = 1.01$ mJy beam $^{-1}$). ALMA 1.05 mm continuum contours are overplotted in white at 5σ , 8σ , 16σ , 64σ , and 600σ (where $\sigma = 0.25$ mJy beam $^{-1}$). Magenta crosses mark the positions of 44 GHz Class I CH_3OH masers from Cyganowski et al. (2009). Each synthesized beam, and a 1 arcsec scale bar, are plotted in the bottom left and bottom right of each panel, respectively.

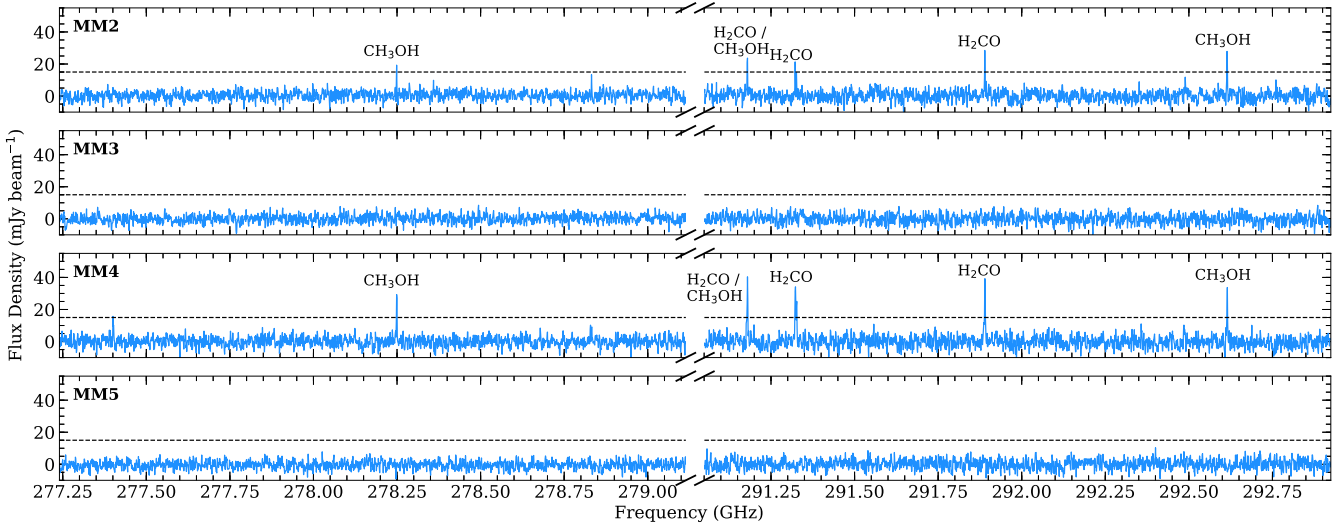


Figure 8. ALMA spectra towards the 1.05 mm continuum peaks of MM2, MM3, MM4, and MM5 (Table 3) for the two broad spectral windows. The break in the frequency axis between the two broad spectral windows is marked by the bold black lines. The 5σ level (where $\sigma = 3$ mJy beam $^{-1}$, Section 2.1) is marked by the horizontal dashed black line. Lines with emission $> 5\sigma$ are labelled.

4a) is coincident with all four new millimetre sources; however, given the emission does not morphologically resemble the ALMA 1.05 mm continuum, it is unlikely to arise from the same volumes as MM2...MM5. As shown in Fig. 4(f), DCN(4 – 3) does exhibit an emission morphology similar to the ALMA 1.05 mm continuum. MM2 and MM4 are detected in emission at the 10σ and 9σ levels respectively (where $\sigma = 6.3$ mJy beam $^{-1}$) and do not exhibit signs of self-absorption (unlike MM1, see Section 3.2.2), while MM3 and MM5 are undetected to a 5σ limit of 31.5 mJy beam $^{-1}$. The positions of peak DCN emission towards MM2 and MM4 are offset from their corresponding ALMA 1.05 mm continuum peaks by 0.09 and 0.40 arcsec, respectively (equivalent to 360 and 1600 au), within a DCN beam (~ 0.47 arcsec; see Table 2). Systemic velocities for MM2 and MM4 are found from Gaussian fitting of the DCN peak emission to be 59.88 ± 0.06 km s $^{-1}$ and 59.72 ± 0.05 km s $^{-1}$, respectively, consistent with the 59.9 ± 1.1 km s $^{-1}$ systemic velocity of MM1 (Cyganowski et al. 2011a), kinematically linking MM2 and MM4 to MM1 and the G19.01–0.03 clump.

A handful of Class I 44 GHz CH_3OH maser spots lie 0.60 arcsec ~ 2400 au to the east of the ALMA 1.05 mm continuum peak of MM4 (see Fig. 4e), coincident spatially and kinematically with H_2CO and CH_3OH emission attributed to the MM1 outflow (see Section 3.2.2). No NH_3 ($J = K = 1, 2, 3, 5, 6, \text{ and } 7$) emission is detected towards, or in the immediate vicinity of, MM2...MM5 in our VLA data, to 5σ limits of $6.2, 5.9, 5.7, 5.5, 4.8, \text{ and } 5.3$ mJy beam $^{-1}$, respectively. Similarly, MM2...MM5 are undetected in the 25 GHz CH_3OH lines in our VLA observations (5σ limits $5.2, 5.1, 4.3, \text{ and } 6.0$ mJy beam $^{-1}$ for the $3_2, 5_2, 8_2, \text{ and } 10_2$ lines). The CH_3OH 5_2 emission spot detected towards the outflow driven by MM1 (see Section 3.2.4) is 3.6 arcsec ~ 14200 au away from the ALMA 1.05 mm continuum peak of MM3. In all, with no clear evidence for protostellar activity in MM2...MM5 in our ALMA and VLA data, the current evidence suggests that these sources may be starless condensations, pre-stellar cores, millimetre knots in MM1’s outflow lobes, or a combination of the three (see also Section 4.2).

4 DISCUSSION

4.1 Physical properties of MM1 from CH₃OH emission

In the following section, we estimate the column density and temperature of MM1 from the observed CH₃OH emission using two complementary methods: (i) a rotation diagram analysis (Section 4.1.1) and (ii) a set of synthetic spectra that represent the observed emission (Section 4.1.2).

4.1.1 Rotation diagram analysis of CH₃OH

Assuming local thermodynamic equilibrium and optically thin emission, a single temperature may describe the emission of all observed lines. This temperature is defined by the Boltzmann distribution, written as:

$$\log\left(\frac{N_u}{g_u}\right) = \log\left(\frac{N}{Q(T_{\text{rot}})}\right) - \frac{E_u}{k_B T_{\text{rot}}}, \quad (1)$$

where N_u is the upper energy level column density, g_u is the upper energy state degeneracy, N is the total column density, $Q(T_{\text{rot}})$ is the partition function, E_u is the upper level energy, k_B is the Boltzmann constant, and T_{rot} is the rotational temperature (e.g. Goldsmith & Langer 1999). The left-hand side of equation (1) may be re-written as:

$$\log\left(\frac{N_u}{g_u}\right) = \log\left(\frac{3k_B \int T_{\text{mb}} dV}{8\pi^3 \nu S_{ij} \mu^2}\right), \quad (2)$$

where $\int T_{\text{mb}} dV$ is the integrated line strength over velocity with units of $\text{K} \times \text{km s}^{-1}$, ν is the rest frequency of the transition, μ is the permanent dipole moment with units of Debye, and S_{ij} is the unit-less intrinsic line strength (e.g. Cummins, Linke & Thaddeus 1986; Herbst & van Dishoeck 2009). When multiple lines of a species are detected, assuming that their emission arises from the same physical structure, and assuming that all lines are optically thin, one may construct a rotation diagram by plotting $\log(N_u/g_u)$ against E_u/k_B . Fitting a straight line will yield T_{rot} from the slope, and $N/Q(T_{\text{rot}})$ from the y-intercept. If a straight line reasonably fits the rotation diagram, the assumption is made that all transitions are thermalized, and thus T_{rot} is expected to equal the excitation temperature, T_{ex} (e.g. Goldsmith & Langer 1999). Taking this T_{rot} , the total column density (N) may be found with the partition function, which, following Townes & Schawlow (1955) and Purcell et al. (2009), for example, may be written for CH₃OH as:

$$Q(T_{\text{rot}}) = 1.2327 T_{\text{rot}}^{1.5}. \quad (3)$$

The most detected species towards MM1 in our spectral tuning at $>5\sigma$ is CH₃OH, with 13 transitions identified across both the wide and narrow bands (see Section 3.2.1) with E_u/k_B ranging 32–736 K. We produce a rotation diagram towards the ALMA 1.05 mm continuum peak of MM1 (Table 3) using eleven CH₃OH transitions, excluding the CH₃OH(15_{1,0} – 14_{2,0}) line from the wide bands, and CH₃OH(6_{1,2} – 5_{1,2}) from the narrow bands, as they are significantly blended by the H₂CO(4_{2,3}–3_{2,2}) and CH₃OCHO(27_{1,27} – 26_{0,26}) lines respectively. We include both A and E transitions in this analysis since we do not detect enough transitions to fit them separately. The integrated intensity of each line is evaluated from Gaussian profiles fitted to the CH₃OH spectra at the ALMA 1.05mm continuum peak position (see Table 3). Errors on the Gaussian fits are propagated through to the rotation diagram, and the best fit is found following a weighted least-squares fit. This rotation diagram is shown in Fig. 9(a), where it can be seen that two data points (marked white, belonging to the CH₃OH(6_{1,5} – 5_{1,4}) and CH₃OH(9_{-1,9} – 8_{0,8}) lines with $E_u/k_B = 63.7$ and 110.0 K respectively) deviate from the general trend

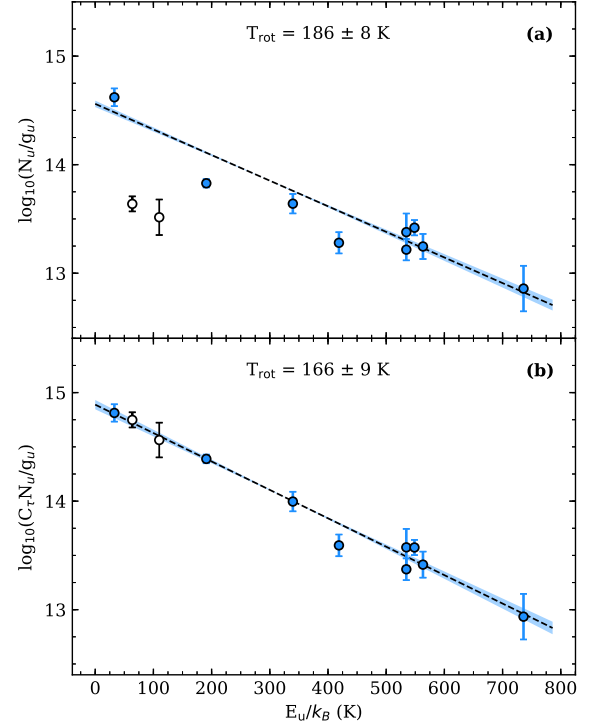


Figure 9. Rotation diagram of CH₃OH at the ALMA 1.05 mm dust continuum peak of MM1, (a) before opacity correction, and (b) following opacity correction. The best fit is shown by the dashed black line, with the statistical uncertainty on the slope and y-intercept represented by the shaded blue region. The CH₃OH(6_{1,5} – 5_{1,4}) and CH₃OH(9_{-1,9} – 8_{0,8}) lines (with $E_u/k_B = 63.7$ and 110.0 K, respectively) are coloured in white as they are outflow tracers (see Fig. 4) and optically thick.

of the other nine lines. These lines are seen in Fig. 4 to be outflow tracing, and their generally low $\log(N_u/g_u)$ is an indication that they may also be optically thick. The derived rotational temperature is 186 ± 8 K.

As previously stated, a rotation diagram is constructed under the assumption that all lines are optically thin. Optically thick lines can inflate derived rotational temperatures due to an artificially shallow slope (e.g. Goldsmith & Langer 1999). We counter this by applying an opacity correction, $C_{\tau_i} = \tau_i / (1 - e^{-\tau_i})$, where the subscript i refers to the i^{th} CH₃OH transition. We follow Brogan et al. (2007, 2009) by iteratively solving for the τ_i and T_{rot} values that produce the best fit, minimizing the χ^2 value. Fig. 9(b) shows the best-fitting opacity-corrected rotation diagram. The τ_i values for this best-fitting range between ~ 0.4 and 11.7, with indeed the CH₃OH(6_{1,5} – 5_{1,4}) and CH₃OH(9_{-1,9} – 8_{0,8}) lines being the most optically thick (with $\tau = 11.7$ and 11.3, respectively). The highest-J, CH₃OH(23_{4,19} – 22_{5,18}) line with $E_u/k_B = 736$ K is unsurprisingly the most optically thin. Of the lines with compact emission morphologies (i.e. that trace MM1 and not the outflow) in the 278 GHz wideband spectral window, the CH₃OH(14_{4,10} – 15_{3,12}) line is the most optically thick, with $\tau = 1.9$, implying an emitting region of $\sim 0'.25 \sim 1000$ au (following Section 4.4 of Brogan et al. 2009). The derived opacity-corrected rotational temperature is 166 ± 9 K, and the column density is $(2.0 \pm 0.4) \times 10^{18} \text{ cm}^{-2}$.

4.1.2 Synthetic CH₃OH spectra

We make a second estimate of the column density and temperature of MM1 by producing synthetic spectra that are representative of the

observed data using the WEEDS extension (Maret et al. 2011) of the CLASS software. WEEDS solves the radiative transfer equation assuming a state of LTE and takes into account the background continuum emission. Using values for the frequency, Einstein A coefficients, partition function, and upper level degeneracy and energy from the JPL and CDMS catalogues (Pickett et al. 1998; Müller et al. 2001), WEEDS calculates the opacity of each line, meaning that corrections such as line broadening are applied to optically thick lines. The free parameters of the synthetic spectra are the column density, excitation temperature, systemic velocity, FWHM velocity width, and source size. The projected diameter of the telescope is also required to calculate the beam dilution/filling factor. We refer the reader to Maret et al. (2011) for a more detailed description of the full procedure.

We explore the posterior distribution of the free parameters of the LTE line models using the Python package EMCEE (Foreman-Mackey et al. 2013), an affine-invariant Monte Carlo Markov Chain (MCMC) sampler (Goodman & Weare 2010). A posterior distribution of model parameters consistent with the data is evaluated by multiple ‘walkers’, allowed to walk for a number of iterations. A ‘burn-in’ period of n_{burn} iterations allows the walkers to converge on the posterior region. These ‘burn-in’ solution chains are then discarded before beginning a ‘production’ run with walkers initialized around the posterior region identified during the burn-in. Walkers are allowed to walk through the posterior for $n_{\text{prod}} > n_{\text{burn}}$ iterations, to allow probing of the covariance of the model parameters. The model parameters that are most representative of the data are found following the maximization of the log-likelihood function:

$$\mathcal{L}(T_{\text{mb}}|\theta) = -0.5 \sum_i \left(\frac{T_{\text{mb},i}^{\text{mod}} - T_{\text{mb},i}^{\text{obs}}}{\sigma_{\text{rms}}^{\text{obs}}} \right)^2, \quad (4)$$

where θ are the model parameters, $T_{\text{mb},i}^{\text{mod}}$ and $T_{\text{mb},i}^{\text{obs}}$ are the model and observed main-beam brightness temperature of the i^{th} channel, respectively, and $\sigma_{\text{rms}}^{\text{obs}}$ is the observed rms noise of the spectrum (see Section 2.1). The statistical uncertainty on each model parameter is evaluated from the 0.16 and 0.84 quantiles of the posterior (i.e. the 1σ level). Our scripts are publicly available² and are packaged together in a reusable form we call WEEDSPY_MCMC where they are generalized to take in user-defined parameters such as the priors, number of walkers, initial walker positions within the parameter space, and the number of burn-in and production iterations, from a text file. A CLASS-readable text file is created containing the θ model parameters currently walked to and the name of the molecule to be modelled, and then a CLASS script is called that runs the LTE model for those θ . Plots are generated of the highest likelihood synthetic spectrum, the corner plot of the 1D and 2D posterior distributions of the free parameters (as in Fig. 10a), and the trace plot of the EMCEE walkers through the parameter space. To efficiently sample the probability distributions for the free parameters of the synthetic spectra generated with WEEDS, spectral windows are treated separately in our scripts.

4.1.3 Pixel-by-pixel analysis of CH₃OH synthetic spectra

Applying this procedure to our ALMA data, we find the highest likelihood model on a pixel-by-pixel basis across MM1, allowing investigation of any spatial variation in the column density, temperature, centroid velocity, and velocity width. As in Section 4.1.1, this analysis focuses on CH₃OH emission, as it is the species with the

highest number of identified transitions in our tuning. Of the thirteen total CH₃OH lines in the tuning, seven are located in the ~ 278 GHz band, four are in the ~ 292 GHz band (see Fig. 3 and Table 4), one lies in the narrow spectral window that targets N₂H⁺(3–2), and one lies in the narrow spectral window that targets DCN(4–3). As the CH₃OH(6_{1,5}–5_{1,4}) and CH₃OH(9_{-1,9}–8_{0,8}) lines (with $\nu_{\text{rest}} = 292.67291$ and 278.30451 GHz respectively) are shown in Fig. 4 to be outflow tracing, we exclude them from this analysis since an assumption made here is that the emitting region is the same for all modelled transitions. We also exclude the CH₃OH(15_{1,0}–14_{2,0}) line ($\nu_{\text{rest}} = 291.24057$ GHz) as it is heavily blended by a close-by H₂CO line (see also Section 4.1.1), the CH₃OH(6_{1,2}–5_{1,2}) line ($\nu_{\text{rest}} = 289.62430$ GHz) as it is blended with a CH₃OCHO line (see Sections 3.2.1 and 4.1.1), and the CH₃OH(10_{1,10}–9_{0,9}) line ($\nu_{\text{rest}} = 292.51744$ GHz) as it is the only identified line in the first torsionally excited state (i.e. $\nu_t = 1$). This leaves six lines in the ~ 278 GHz band, one line in the ~ 292 GHz band, and one line in a narrow band. Since modelling one line is not sufficient to constrain four free parameters, we conduct our MCMC analysis on the six remaining CH₃OH lines in the ~ 278 GHz band (indicated in bold in Table 4). We then use the best-fitting parameters to generate synthetic spectra for the other spectral windows and check the resulting spectra for goodness of fit (see also Section 4.3.1).

For our pixel-by-pixel modelling, we fix the source size to the geometric mean of the ~ 278 GHz synthesized beam (~ 0.5 arcsec).³ We also limit the pixel area being modelled to within the continuum source size of MM1 from Table 3 (see white contour in Figs 11a and b), shown in Paper I to match well the region of compact molecular line emission (see their Fig. 3). The projected diameter of the ALMA array was calculated to be 558 metres⁴, and we estimate the background continuum on a pixel-by-pixel basis (McGuire et al. 2018), with the ALMA 1.05 mm continuum converted to brightness temperature.⁵ We initialize 60 walkers, and allow them to run for $n_{\text{burn}} = 200$ and $n_{\text{prod}} = 500$ iterations (see Appendix B for a discussion of these choices). The remaining free parameters are the column density, excitation temperature, systemic velocity and FWHM velocity width. We assume uniform, uninformative priors, and initialize the walkers in a four-dimensional sphere about an initial value that lies within those priors. Our priors are estimated from initial ‘dummy’ runs of the LTE synthetic spectra outside of WEEDSPY_MCMC, and are set to be $(0.05\text{--}3.0) \times 10^{18} \text{ cm}^{-2}$ for the column density, 80–300 K for the temperature, 56.0–64.0 km s⁻¹ for the centroid velocity, and 2.0–8.0 km s⁻¹ for the velocity width.

Fig. 10(a) shows the 1D and 2D posterior distributions of column density, temperature, centroid velocity, and velocity width, evaluated for the spectrum at the ALMA 1.05 mm continuum peak of MM1. The narrow, normally distributed 1D posteriors for column density, temperature and centroid velocity show that these parameters are reasonably constrained. The slope in the 2D column density–temperature posterior distribution indicates an unsurprising, but only slight, degeneracy between these two parameters, meaning the statistical errors are small despite this. There is no obvious covariance of the centroid velocity with either column density or temperature.

³The image cube is converted to brightness temperature using the Rayleigh–Jeans approximation and beamsize with the `tt.brightnessImage` function of TODDTOOLS.

⁴Calculated using the `au.getBaselineLengths` function from the ANALYSISUTILS PYTHON package.

⁵Conversion done under the Rayleigh–Jeans approximation using the `tt.brightnessImage` function of TODDTOOLS.

²https://github.com/gwen-williams/WeedsPy_MCMC

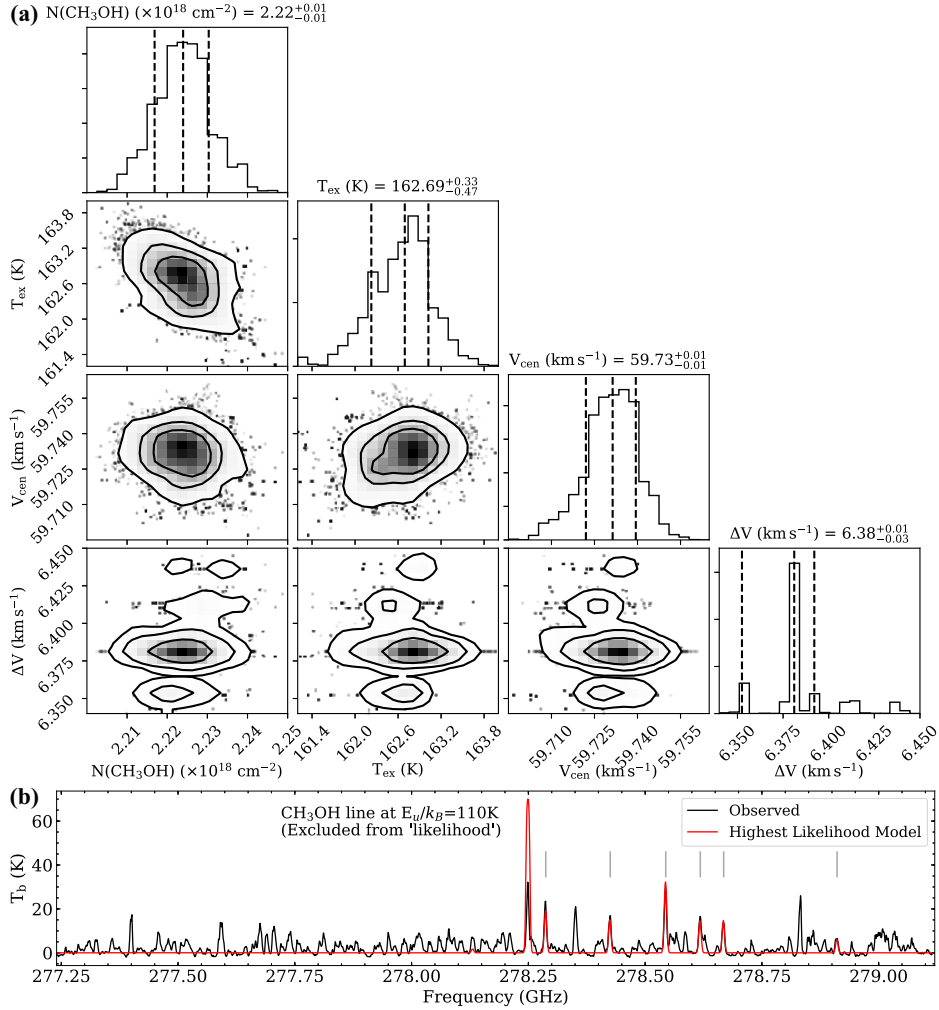


Figure 10. (a) One-dimensional and two-dimensional histograms of the posterior distributions for the free parameters in the LTE synthetic spectral modelling ($N(\text{CH}_3\text{OH})$, T_{ex} , V_{cen} , and ΔV) towards the ALMA 1.05 mm continuum peak. Black contours on the 2D histograms are placed at 2σ , 1.5σ , and 1σ , while the dashed black lines on the 1D histograms are placed at the 0.16, 0.5, and 0.84 quantiles. (b) Observed spectrum towards the ALMA 1.05 mm continuum peak (black) overplotted with the corresponding highest likelihood model (red) i.e. model parameters defined by the mode of the posterior, printed in panel (a). The six CH_3OH lines that are modelled and included in the maximization of the log-likelihood function are marked by vertical grey lines. The excluded $\text{CH}_3\text{OH}(9_{-1,9} - 8_{0,8})$ line with $E_u/k_B = 110.0$ K is labelled.

The velocity width is less well constrained, with two slight peaks around the mode of the posterior distribution (within $<0.03 \text{ km s}^{-1}$). Though significantly smaller than the spectral resolution of our data ($\sim 1 \text{ km s}^{-1}$), this uncertainty is attributed to line blending rather than undersampling as the double peak persists in tests where n_{prod} is increased to >3000 . The double peak also persists when walkers are initialized with a different random number seed, so is independent of initial walker position. The highest likelihood model spectrum at the continuum peak position of MM1 is shown in Fig. 10(b), with parameters $N(\text{CH}_3\text{OH}) = (2.22 \pm 0.01) \times 10^{18} \text{ cm}^{-2}$, $T_{\text{ex}} = 162.7^{+0.3}_{-0.5}$ K, $V_{\text{cen}} = 59.73 \pm 0.01 \text{ km s}^{-1}$, and $\Delta V = 6.38^{+0.01}_{-0.03} \text{ km s}^{-1}$. These remain unchanged (within the errors) when walkers are initiated with a different random number seed, and when n_{prod} is increased to >3000 . These column density and temperature values are remarkably consistent with those derived from the opacity-corrected rotation diagram of $(2.0 \pm 0.4) \times 10^{18} \text{ cm}^{-2}$ and 166 ± 9 K, respectively (see Section 4.1.1), and the centroid velocity is also consistent with the known systemic velocity of $59.9 \pm 1.1 \text{ km s}^{-1}$ (Cyganowski et al. 2011a). The line optical depths returned by CLASS are lower than

those estimated in the rotation diagram analysis with an average $\tau = 0.3$ compared to $\tau = 1.0$ (excluding $\text{CH}_3\text{OH}(9_{-1,9} - 8_{0,8})$ with $E_u/k_B = 110.0$ K). We attribute the higher line opacities estimated from the rotation diagram to the source size not being fixed in the rotation diagram approach (see Section 4.1.1). Fig. 10(b) shows the synthetic spectrum well reproduces the observed CH_3OH emission, other than significantly overestimating the line strength of the optically thick, outflow tracing $\text{CH}_3\text{OH}(9_{-1,9} - 8_{0,8})$ line (see Fig. 4) that was excluded from the maximization of the log-likelihood. This vindicates its exclusion from the analysis, further suggesting that the emission from the $\text{CH}_3\text{OH}(9_{-1,9} - 8_{0,8})$ line may not occur in the same volume as the other modelled, optically thin lines.

4.1.4 Images of CH_3OH physical parameters

Maps of the pixel-by-pixel, highest likelihood CH_3OH model parameters towards MM1 are shown in Fig. 11. The highest likelihood centroid velocity map (Fig. 11a) shows a clear gradient in velocity

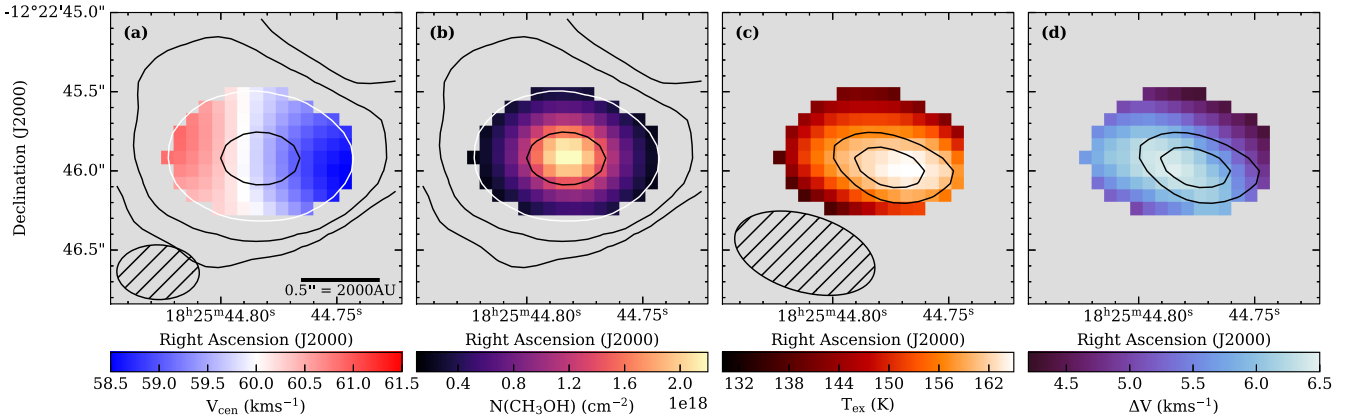


Figure 11. Pixel-by-pixel highest likelihood model parameters from the WEEDS CH₃OH synthetic spectra towards MM1: (a) centroid velocity in km s⁻¹, (b) CH₃OH column density in cm⁻², (c) excitation temperature in Kelvin, and (d) FWHM velocity width in km s⁻¹. ALMA 1.05 mm continuum contours are plotted in panels (a) and (b) at 8, 16, 64, and 200σ (where σ = 0.25 mJy beam⁻¹). The white contour (at 64σ) represents the level above which pixels were fed into WEEDSPY_MCMC, and matches the source size of MM1 (see Table 3). Contours of VLA 5.01 cm emission (from Paper I) are plotted in panels (c) and (d) at the 4σ and 5σ levels (where σ = 5.0 μJy beam⁻¹) in panel. A scale bar and the ALMA beam are plotted in panel (a), and the VLA beam is plotted in panel (c).

across MM1 in agreement with the gradient reported in Paper I from a simpler moment analysis of individual lines. The CH₃OH column density (Fig. 11b) peaks coincident with, and follows the same morphology as, the ALMA 1.05 mm continuum emission. The position of peak CH₃OH temperature (18^h25^m44^s.763 – 12°22′46″.00 (J2000); see Fig. 11c) is however offset from the ALMA 1.05 mm dust continuum and CH₃OH column density peaks by 0.22 arcsec ~ 880 au. While the column density and temperature are somewhat degenerate (see Fig. 10a), the difference between the offset peak temperature (165.5 ± 0.6 K) and the temperature at the column density peak (162.7 ± 0.4 K) is significantly greater than its propagated statistical error (i.e. 2.8 ± 0.7 K). In Paper I, a centimetre counterpart to MM1 (called CM1) was detected for the first time with the VLA at 5.01 and 1.21 cm. The VLA 1.21 cm emission peak was coincident with the ALMA 1.05 mm continuum peak of MM1, whilst the VLA 5.01 cm emission peak of CM1 (18^h25^m44^s.773 – 12°22′46″.00 (J2000); Paper I) was found to be offset from MM1 by 0.16 arcsec ~ 640 au (Paper I). Indeed, the entire morphology of the region of elevated CH₃OH temperature matches that of the VLA 5.01 cm emission, with both being elongated along a south-easterly direction relative to MM1 (as shown in Fig. 11c). The velocity width map in Fig. 11(d) also shows a similar elongation to the VLA 5.01 cm continuum, however it does not peak coincident with either the CH₃OH column density, the CH₃OH temperature, nor the VLA 5.01 cm continuum position. Following analysis of the combined centimetre-millimetre SED of CM1/MM1 in Paper I, it was revealed that a free-free emission component was required to describe the VLA 5.01 cm emission. This component was interpreted as a small, 66 au diameter gravitationally trapped hypercompact (HC) HII region, which directly implies the presence of a source causing ionization and heating of its surroundings. Given that the morphology of the elevated CH₃OH temperature aligns with that of the VLA 5.01 cm continuum, and that the position of peak CH₃OH temperature is only offset from the VLA 5.01 cm position of CM1 by 0.07 arcsec ~ 280 au (equivalent to the absolute positional uncertainty of the VLA 5.01 cm data of 0.07 arcsec; Paper I), it is reasonable to surmise that both are attributable to the same underlying source/mechanism. We further speculated in Paper I that the VLA 5.01 cm emission being misaligned with respect

to the direction of the bipolar outflow emanating from MM1 was suggestive of the ionization being driven by a second object, perhaps indicative of an unresolved high-mass binary system. In that case, a second possible origin for the offset elevated CH₃OH temperature could be the presence of an ionized jet driven by the unresolved high-mass binary companion. Outflows and jet-like outflows are noted in the literature to cause heating of molecular gas (e.g. Zhang et al. 2007; Wang et al. 2012).

4.2 Physical properties of MM1...MM5 from dust emission

As mentioned in Sections 1 and 4.1.4, it was shown in Paper I from an analysis of the centimetre-millimetre SED of MM1 that its ALMA 1.05 mm flux was 99.99 per cent dominated by thermal dust emission. MM2...MM5 are also likely dominated by thermal dust emission, given their non-detection in the centimetre at 1.21 and 5.01 cm with the VLA to 5σ limits of 30 and 25 μJy beam⁻¹, respectively (Paper I). As such, the masses (M_{gas}) of MM1...MM5 may be calculated from their integrated flux densities at 1.05 mm (S_{1.05 mm}) assuming isothermal dust emission following Hildebrand (1983):

$$M_{\text{gas}} = \frac{d^2 R S_{1.05 \text{ mm}} C_{\tau_{\text{dust}}}}{\kappa_{1.05 \text{ mm}} B_{\nu}(T_{\text{dust}})}, \quad (5)$$

where d is the distance, R is the gas-to-dust mass ratio (here assumed to be 100), $\kappa_{1.05 \text{ mm}}$ is the dust opacity at 1.05 mm, $B_{\nu}(T_{\text{dust}})$ is the Planck function, and T_{dust} is the dust temperature. We include a correction for dust optical depth, $C_{\tau_{\text{dust}}}$ as:

$$C_{\tau_{\text{dust}}} = \tau_{\text{dust}} / (1 - e^{-\tau_{\text{dust}}}), \quad (6)$$

where τ_{dust} may be estimated as:

$$\tau_{\text{dust}} = -\ln \left(1 - \frac{T_b}{T_{\text{dust}}} \right). \quad (7)$$

We estimate T_b as the mean brightness temperature across the size of each source (as listed in Table 3), though this may underestimate τ_{dust} for small-scale structures. From Ossenkopf & Henning (1994), we set $\kappa_{1.05 \text{ mm}} = 1.45 \text{ cm}^2 \text{g}^{-1}$ for dust grains with thick ice mantles

Table 6. Derived properties for mm continuum sources.

Source	T_b (K)	T_{dust} (K)	τ_{dust}	M_{gas} (M_{\odot})	$N(\text{H}_2)$ $\times 10^{23}$ (cm^{-2})	$n(\text{H}_2)$ $\times 10^6$ (cm^{-3})
MM1	10.9	163	0.07	4.3	6.7	17.0
MM2	3.5	24	0.16	1.3	3.2	10.3
		15	0.27	2.7	6.6	21.1
MM3	3.0	24	0.13	1.0	1.5	3.9
		15	0.22	2.1	3.1	7.8
MM4	2.9	24	0.13	0.9	1.4	3.4
		15	0.22	1.8	2.7	6.8
MM5	2.8	24	0.13	0.1	–	–
		15	0.21	0.2	–	–

Column 1: Source name. Column 2: Planck brightness temperature averaged over the source size listed in Table 3. Column 3: Assumed dust temperature, derived from the LTE synthetic spectra for MM1 (see Section 4.1.3), and a temperature range of 15–24 K assumed for MM2...MM5 based on large-scale clump observations (Schuller et al. 2009; Cyganowski et al. 2013; Elia et al. 2017). Column 4: Dust optical depth, calculated from the average T_b in column 2. Column 5: Opacity-corrected gas mass, in solar masses. Column 6: H_2 column density, and Column 7: H_2 volume density, both assuming spherical symmetry.

in high-density gas (as in Paper I; Cyganowski et al. 2017). We also assume that the dust is well-coupled to the gas such that $T_{\text{dust}} = T_{\text{gas}}$. The temperatures we assume for each of the sources is discussed below in Sections 4.2.1 and 4.2.2. Assuming spherical geometry, a mean molecular weight per hydrogen molecule (μ_{H_2}) of 2.8 (e.g. Kauffmann et al. 2008), and a radius equal to half the geometric mean of the source sizes presented in Table 3, we further calculate the average H_2 column density and H_2 volume density. All derived source properties are listed in Table 6.

4.2.1 Temperature, mass, and stability of MM1

In Paper I, we assumed a temperature range for MM1 of 100–130 K based on the $\text{CH}_3\text{CN}(J=12-11)$ line fitting of Cyganowski et al. (2011a) from $2.3''$ angular resolution SMA data. Our new ALMA data (with $0.4''$ angular resolution) improves on that by a factor of ~ 30 in beam area. We revise our temperature assumption to 163 K, as calculated at the ALMA 1.05 mm continuum peak of MM1 in Section 4.1.3 from the CH_3OH synthetic spectra. This is an increase of 33–66 K from the SMA-derived temperature. Observations of the EGO G11.92–0.61 (hereafter G11.92) by both Cyganowski et al. (2011a) and Ilee et al. (2016) provide us with a point of comparison on temperature. With 2.4 arcsec angular resolution SMA observations, Cyganowski et al. (2011a) derived 77 and 166 K temperatures for G11.92 from a two-component fit to CH_3CN emission. Taking the same approach but with 0.5 arcsec angular resolution SMA observations (a factor of ~ 27 improvement in beam area), Ilee et al. (2016) find the two G11.92 temperature components to be 150 and 230 K. This is an increase of 60–70 K in temperature, attributed to the difference in probed spatial scales between the two data sets. The same resolution-dependent behaviour is observed here for the temperature of G19.01 MM1.

The mass of MM1 is here revised, from $M_{\text{gas}} = 5.4\text{--}7.2 M_{\odot}$ at 130–100 K derived in Paper I, to $M_{\text{gas}} = 4.3 M_{\odot}$ at 163 K (Table 6). Attributing this gas mass to the now known circumstellar disc around MM1, the stability of the disc can be assessed by estimation of the disc-to-star mass ratio (as done in Paper I), with unstable discs exhibiting typical values of $M_{\text{gas}}/M_{*} > 0.1$ (e.g. Kratter & Lodato

2016). Following Paper I, the stellar mass (M_{*}) can be calculated as $M_{*} = M_{\text{enc}} - M_{\text{gas}}$ where M_{enc} is the enclosed mass within the disc outer radius (estimated as $\sim 40\text{--}70 M_{\odot}$ from kinematic modelling in Paper I). The disc-to-star mass ratio was found in Paper I to be $\sim 0.08\text{--}0.22$ hinting that the disc could be unstable and be undergoing fragmentation into as-of-yet undetected low-mass stellar companions. It was noted, however, that should the temperature of MM1 increase on the size-scales probed by the ALMA data (as it did for the SMA observations of G11.92; Cyganowski et al. 2011a; Ilee et al. 2016), then the resulting lower M_{gas} could push the disc towards stability. Our revised M_{gas}/M_{*} is 0.07–0.12, indeed indicative of the disc being potentially stable against fragmentation. This approach does, however, risk underestimating the disc mass, as it does not account for variations in the temperature, dust opacity and dust optical depth in the disc (Johnston et al. 2015; Forgan et al. 2016).

4.2.2 Low mass protocluster members

As there are insufficient molecular lines detected with ALMA towards MM2...MM5 for the estimation of temperature, we use clump-scale observations of G19.01 to inform our temperature assumptions. Elia et al. (2017) derive $T_{\text{dust}} = 17.9$ K from SED fitting of HI-GAL observations, while Schuller et al. (2009) and Wien et al. (2012) derive $T_{\text{gas}} = 19.5$ K from NH_3 hyperfine structure fitting of ~ 40 arcsec angular resolution Effelsberg 100 m data. Cyganowski et al. (2013) also estimated temperature for the G19.01 clump using NH_3 observations, taken with the Nobeyama 45 m telescope. Their single-temperature fit to the NH_3 spectra yielded a kinetic temperature of 23.8 ± 0.4 K, but they found that a two-component fit with $T_{\text{kin, cool}} = 14.7 \pm 0.5$ K and $T_{\text{kin, warm}} = 50.2 \pm 4.4$ K better represented the observed data (Cyganowski et al. 2013). As the warm ~ 50 K component is likely attributable to the central MYSO (MM1), we exclude it and use the remaining temperature estimates to inform an assumed temperature range for MM2...MM5 of 15–24 K. Table 6 lists derived properties for $T_{\text{dust}} = 15$ and 24 K. We note that H_2 column and volume densities are not included for MM5 as its size is smaller than a beam.

The gas masses of MM2...MM5 range between 0.1 and $1.3 M_{\odot}$ and 0.2 and $2.7 M_{\odot}$ at 24 and 15 K, respectively (see Table 6), and their median radius is ~ 2000 au (excluding the unresolved MM5; see Table 3). As such, the physical properties of these millimetre sources appear consistent with typical low-mass pre/protostellar cores observed in IRDCs (with masses and radii of a few solar masses and a few thousand au, respectively, e.g. Sanhueza et al. 2019; Morii et al. 2021; Redaelli et al. 2022) rather than discs around low-mass YSOs (with masses and radii $< 0.1 M_{\odot}$ and a few hundred au, respectively, e.g. Dullemond et al. 2018; Huang et al. 2018). Furthermore, their lack of COM emission or signs of outflow activity indicate that they may be candidate low-mass pre-stellar rather than protostellar cores. Interestingly, this result contrasts with the situation in the EGO G11.92 – 0.61, where several of the low-mass cores identified by Cyganowski et al. (2017) drive molecular outflows, clearly identifying them as protostellar cores.

The number and spatial distribution of the low-mass cores in G19.01–0.03 also contrasts with G11.92–0.61, where Cyganowski et al. (2017)’s 1.05 mm ALMA observations of the ATLASGAL clump detected 16 new compact mm continuum sources (for a total of 19, including three previously known massive sources). Compared to G11.92–0.61, the low-mass sources detected in G19.01–0.03

are located closer to the most massive member of the protocluster (median projected separation ~ 0.08 pc compared to ~ 0.17 pc) and comprise a lower fraction of the clump mass (< 1 per cent compared to 3–5 per cent; Cyganowski et al. 2017). We consider our results in the context of expectations for thermal Jeans fragmentation. For the simple assumption of a uniform density sphere, the minimum mass necessary for a fragment to be bound, and so collapse, is

$$M_J = \left(\frac{5c_s^2}{2G} \right)^{3/2} \left(\frac{3}{4\pi\rho} \right)^{1/2}, \quad (8)$$

where ρ is the density, and c_s is the sound speed defined as:

$$c_s = \left(\frac{k_B T}{\mu_{H_2} m_H} \right)^{1/2}, \quad (9)$$

where μ_{H_2} is the mean molecular weight per hydrogen molecule (equal to 2.8; see also Section 4.2), and m_H is the mass of a Hydrogen atom. The length scale for a fragment to be bound, under the same assumptions, is the Jeans radius

$$R_J = \left(\frac{15c_s^2}{8\pi G\rho} \right)^{1/2}, \quad (10)$$

where R_J is the radius of a sphere of mass M_J and the Jeans length (λ_J) is $\lambda_J \approx 2R_J$. Using the Hi-GAL clump properties (1165 M_\odot and $R = 0.175$ pc when scaled to $D = 4$ kpc, $T = 17.9$ K; Section 1, Elia et al. 2017), we calculate the thermal Jeans radius and thermal Jeans mass of the G19.01–0.03 clump to be $R_J \approx 0.012$ pc and $M_J \approx 0.36 M_\odot$, respectively. Using the ATLASGAL clump properties (926 M_\odot and $R = 0.358$ pc for $D = 4.0$ kpc, $T = 19.5$ K, Section 1, Schuller et al. 2009), $R_J \approx 0.041$ pc and $M_J \approx 1.36 M_\odot$. The linear resolution of our ALMA data is ~ 0.008 pc, and the 5σ detection limit (converted to mass) is 0.1 – $0.3 M_\odot$ at 24–15 K, so we are sensitive to the relevant fragmentation scales. With median masses of 1.0 – $2.0 M_\odot$ at 24–15 K, respectively, MM2...MM5 are of order the thermal Jeans mass, consistent with the results of Palau et al. (2015) from their study of mm fragments within the inner 0.1 pc of ~ 20 massive dense cores. The number of millimetre sources detected in G19.01 is, however, notably lower than expected for thermal Jeans fragmentation. For the 13 per cent core formation efficiency (CFE) found by Palau et al. (2015), $N_{\text{Jeans}} = (M_{\text{clump}} \text{CFE})/M_J \sim 420$ and ~ 90 for the Hi-GAL and ATLASGAL-based estimates, respectively. Strong magnetic fields are expected to suppress fragmentation, and recent observational work found a tentative correlation between the number of mm fragments and the mass-to-flux ratio for a sample of 18 massive dense cores with polarization data (Palau et al. 2021, and references therein). Observations of polarized dust emission in G19.01–0.03 are needed to assess whether a dynamically important magnetic field contributes to the low level of observed fragmentation.

4.2.3 Virial analysis of MM4

The virial parameter (α_{vir}) is a commonly used diagnostic in determining the boundedness of structures. To qualify as a stellar progenitor, a source must be in a gravitationally bound state. This is satisfied by $\alpha_{\text{vir}} < 2$ in the absence of pressure terms such as magnetic energy density. Furthermore, a core is said to be in hydrostatic equilibrium when $\alpha_{\text{vir}} \sim 1$, or to be gravitationally unstable when $\alpha_{\text{vir}} < 1$. The virial parameter is often expressed as follows:

$$\alpha_{\text{vir}} = \frac{M_{\text{vir}}}{M_{\text{core}}}, \quad (11)$$

where M_{vir} is the virial mass, and M_{core} is the observed core mass. The virial mass for a spherical core may be calculated following MacLaren, Richardson & Wolfendale (1988):

$$M_{\text{vir}} = 3 \left(\frac{5 - 2n}{3 - n} \right) \frac{\sigma_{\text{NT}}^2 R}{G}, \quad (12)$$

where n is the index of the density profile of the source (where $\rho \propto r^{-n}$), R is the radius, and G is the gravitational constant. The non-thermal velocity dispersion, σ_{NT} , may be calculated following:

$$\sigma_{\text{NT}}^2 = \sigma_{\text{obs}}^2 - \sigma_{\text{th}}^2 = \sigma_{\text{obs}}^2 - \frac{k_B T_{\text{dust}}}{\mu m_H}, \quad (13)$$

where σ_{obs} and σ_{th} are the observed and thermal velocity dispersions respectively (Bertoldi & McKee 1992), T_{dust} is the dust temperature (assumed to equal the gas temperature), μ is the molecular weight of the molecular tracer, and m_H is the mass of a Hydrogen atom.

As discussed in Sections 3.2.2 and 3.2.5, of the cold and dense gas tracers we detect it is only the emission from DCN (with $\mu = 28$) that appears morphologically similar to the ALMA 1.05 mm dust continuum emission, with $\geq 5\sigma$ detections towards MM1, MM2 and MM4. As we cannot safely disentangle the DCN emission of MM2 from the surrounding envelope emission (see Fig. 4), we focus our virial analysis on MM4 as it appears isolated. As we aim to test whether MM4 could be a pre-stellar core, we assume a flat density profile where $n = 0$ (e.g. Ward-Thompson et al. 1994). DCN exhibits nuclear quadrupole hyperfine structure, with seven lines in the $J = 4 - 3$ transition with velocity offsets from the main component between -1.6 and 2.1 km s^{-1} (Müller et al. 2001) with a mean velocity offset of 0.1 km s^{-1} (within our 1 km s^{-1} spectral resolution). The effect of these components is most important in the lower energy DCN transitions such as $J = 1 - 0$ or $J = 2 - 1$ (e.g. Parise et al. 2009), with the strongest central component dominating in transitions such as $J = 4 - 3$. We fit the hyperfine structure lines on a pixel-by-pixel basis across MM4 using the *hfs* fitting routine of the CLASS software. We set σ_{obs} to the mean velocity dispersion across the FWHM size of MM4 of $0.58 \pm 0.03 \text{ km s}^{-1}$. Taking the radius as half the geometric mean of the deconvolved size of MM4 listed in Table 3 (equal to ~ 2000 AU), the virial mass of MM4 is calculated to be $3.8 \pm 0.4 M_\odot$. With M_{core} calculated from the 1.05 mm dust emission ($1.84 M_\odot$ at 15 K, or $0.91 M_\odot$ at 24 K; see Table 6), this yields $\alpha_{\text{vir}} = 2.0 - 4.1 (\pm 0.4)$. This indicates that MM4 could be an unbound structure, perhaps a knot in the red-shifted outflow lobe driven by MM1, likely to disperse back into the ISM if internal pressures continue to dominate over gravity. On the other hand, MM4 could be on the cusp of boundedness at the lower end of our temperature range, possibly indicative of the early stages of a pre-stellar core.

4.3 Chemistry of MM1 in context

As discussed in Sections 1 and 3.2.1, the detection of a line forest towards MM1 with ALMA (see Fig. 3) reveals a chemical richness that was lacking in the SMA observations of Cyganowski et al. (2011a). We here estimate the abundances of these newly detected molecular species towards MM1, to see where MM1 sits in relation to other sources in the literature.

4.3.1 Estimation of likely column densities and abundances

In Sections 4.1.2 and 4.1.3, we produced LTE synthetic spectra to evaluate the highest likelihood column density, temperature, centroid

Table 7. Highest likelihood column densities of molecular species identified towards the ALMA 1.05 mm continuum peak of MM1, and their abundances with respect to CH₃OH and H₂, arranged by decreasing column density.

Molecule (X)	N(X) (cm ⁻²)	Fractional abundance	
		N(X)/N(CH ₃ OH)	N(X)/N(H ₂)
CH ₃ OH	2.2×10^{18}	10^0	3.3×10^{-6}
CH ₃ OCH ₃	4.3×10^{17}	2.0×10^{-1}	6.5×10^{-7}
¹³ CH ₃ OH	3.9×10^{17}	1.8×10^{-1}	5.9×10^{-7}
CH ₃ OCHO	1.3×10^{17}	5.9×10^{-2}	2.0×10^{-7}
CH ₃ CH ₂ OH	6.0×10^{16}	2.7×10^{-2}	9.1×10^{-8}
OCS	4.4×10^{16}	2.0×10^{-2}	6.7×10^{-8}
H ₂ CO	3.0×10^{16}	1.4×10^{-2}	4.6×10^{-8}
CH ₃ CHO	1.7×10^{16}	7.7×10^{-3}	2.6×10^{-8}
H ₂ CS	1.6×10^{16}	7.2×10^{-3}	2.4×10^{-8}
CH ₃ CH ₂ CN	1.0×10^{16}	4.6×10^{-3}	1.5×10^{-8}
NH ₂ CHO	5.0×10^{15}	2.3×10^{-3}	7.6×10^{-9}
HC ₃ N	4.4×10^{15}	2.0×10^{-3}	6.6×10^{-9}
¹³ CS	1.5×10^{15}	6.8×10^{-4}	2.3×10^{-9}

Column 1: Molecule name. Column 2: Column density of each identified molecule at the ALMA 1.05 mm continuum peak of MM1 (Table 3). Column 3: Abundance of each molecule with respect to the ¹²CH₃OH column density at the ALMA 1.05 mm continuum peak of MM1 (2.2×10^{18} cm⁻²; Section 4.1.3). Column 4: As for column 3, but for H₂ (6.6×10^{23} cm⁻²; Table 6).

velocity, and velocity width of CH₃OH towards MM1. However, the other detected species listed in Table 4 do not have enough identified transitions for the constraint of four free parameters, nor for the construction of a rotation diagram as in Section 4.1.1. We instead evaluate order of magnitude estimates for the column densities of these species (CH₃OCH₃, ¹³CH₃OH, CH₃CH₂OH, CH₃OCHO, OCS, H₂CO, CH₃CHO, H₂CS, CH₃CH₂CN, NH₂CHO, HC₃N, and ¹³CS) at the ALMA 1.05 mm continuum peak of MM1 by keeping only the column density as a free parameter (e.g. Csengeri et al. 2019) in the EMCEE sampler with WEEDSPY_MCMC. The synthetic spectra for each molecular species are evaluated individually. As in Section 4.1.3, the source size is fixed to the geometric mean of the ~278 GHz synthesized beam (~0.5 arcsec). The temperature, centroid velocity, and velocity width are set to the highest likelihood values evaluated at the ALMA 1.05 mm continuum peak from the CH₃OH spectra (i.e. 162.7 K, 59.7 km s⁻¹ and 6.4 km s⁻¹, respectively, see Fig. 10). As discussed in Paper I, for molecular lines associated with MM1 (i.e. not outflow-tracing) the extent of the line emission is generally consistent across species and with the extent of the 1.05 mm continuum emission (e.g. fig. 3 of Williams et al. 2022). For molecular species with transitions in multiple spectral windows, the synthetic spectra were evaluated in the spectral window with the most transitions. The resulting highest likelihood column density was then used to generate synthetic spectra for the other spectral windows.

The highest likelihood column density of each species is listed in Table 7, and Fig. 12 shows the combined LTE synthetic spectrum for the two wide-band spectral windows for all identified molecular species. On the whole, the combined model reproduces the observed emission well. Some molecular lines appear in the synthetic spectrum that were not listed in Table 4 (or labelled in Figs 3 or 12), which is attributed to overlapping lines from the same and/or multiple species making their unequivocal identification in Section 3.2.1 difficult. Some of the identified transitions have their emission overestimated. These include the CH₃OH(6_{1,5} – 5_{1,4}) and CH₃OH(10_{1,10} – 9_{0,9}) lines (with $\nu_{\text{rest}} = 292.67291$ and 292.51744 GHz, respectively), the former being of an outflow-tracing nature (see Fig. 4) with

an apparently low integrated intensity in the rotation diagram of Fig. 9(a), and the latter being the only transition identified in the tuning to be in the first torsionally excited state. The heavily blended H₂CO(4_{2,3} – 3_{2,2}) and CH₃OH(15_{1,0} – 14_{2,0}) lines (with $\nu_{\text{rest}} = 291.23777$ and 291.24057 GHz, respectively) also have their intensity overestimated, which we attribute to the line blending and the limitations of linearly combining independent models of different species. The H₂CO(4_{2,2} – 3_{2,1}) line ($\nu_{\text{rest}} = 291.94807$ GHz) also has its intensity overestimated, attributed to this line also being heavily blended. Finally, the CH₃OCH₃(16_{1,16} – 15_{0,15}) line ($\nu_{\text{rest}} = 292.41225$ GHz) is overestimated despite all other CH₃OCH₃ lines in the tuning having their intensities well reproduced, and it being shown in Paper I to exhibit compact emission consistent with the other identified lines.

Fractional abundances of each species with respect to CH₃OH and H₂ are evaluated from the ratio of their respective column densities. We take the CH₃OH column density at the ALMA 1.05 mm continuum peak from the synthetic spectra in Section 4.1.3, and the H₂ column density found in Section 4.2 from the ALMA 1.05 mm continuum. As listed in Table 7, we report fractional abundances of the identified species ranging from 10⁻¹ to 10⁻⁴ with respect to CH₃OH, and 10⁻⁶ to 10⁻⁹ with respect to H₂.

4.3.2 Comparison to other YSOs observed at high resolution

To put the methanol column density and these fractional abundances into context, we compare them to values reported in the literature. Collated in Fig. 13 are ALMA observations for both low-mass YSOs and high-mass hot cores that have reported observations of CH₃OH, CH₃OCH₃, and CH₃CHO, and that have rotational temperatures and CH₃OH column densities derived from the main CH₃OH isotopologue. Our MM1 data are overplotted for comparison. Compared to the other high-mass YSOs shown in Fig. 13, the CH₃OH column density, temperature, and CH₃CHO fractional abundance of MM1 appear consistent, while MM1 may be one of the most abundant sources in CH₃OCH₃ (Fig. 13b).

It is also interesting to consider the low- and high-mass sources in Fig. 13 in relation to each other. Of the high-mass sources shown, G10.6–0.4 hot core 1 (Law et al. 2021) has the lowest CH₃OCH₃ and CH₃CHO fractional abundances (Fig. 13b, c), a result of its comparatively low CH₃OCH₃ and CH₃CHO column densities. Of the low-mass sources, IRAS 16293–2422 A (Manigand et al. 2020) has the lowest CH₃CHO fractional abundance (Fig. 13c), and is noted to have more extended CH₃CHO emission morphology compared to the other COMs, whilst SVS13–A VLA4B (Bianchi et al. 2022) exhibits the lowest CH₃OCH₃ abundance (Fig. 13b). However despite these outliers, the general parameter spaces occupied by the low- and high-mass sources in Fig. 13 appear remarkably similar to each other. Regarding the CH₃OH column density and temperature in particular, single-dish observations in the literature have previously reported a distinct separation in these parameters across mass scales. Öberg et al. (2014) for instance with their literature sample show low CH₃OH column density and temperature towards low-mass COM-emitting sources, and high CH₃OH column density and temperature towards high-mass COM-emitting sources. With beam dilution a potential contributing factor to this, Öberg et al. (2014) also collate a handful of resolved SMA observations, noting the distribution to be more continuous rather than separated across mass when including resolved observations. With the more recent ALMA observations collated here, this behaviour is even more pronounced, with the chemistry of low- and high-mass sources appearing similar in this

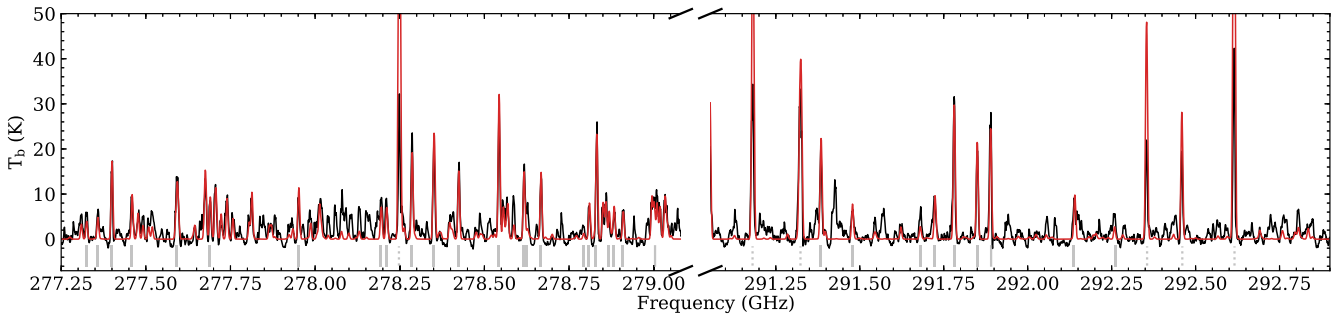


Figure 12. Observed spectra towards the ALMA 1.05 mm continuum peak (black) of MM1, overlaid with the combined highest-likelihood LTE synthetic spectra (red) for all COM species listed in Table 7. Vertical grey lines mark the transitions identified in Section 3.2.1, with dotted lines indicating transitions mentioned in Section 4.3.1 that have overestimated brightness temperatures in the synthetic spectrum.

set of interferometric observations. A similar trend has recently been noted by Chen et al. (2023), who compare the abundance ratios of Oxygen-bearing COMs towards their ALMA sample of 14 high-mass sources with interferometric observations of five low-mass sources from the literature. The Chen et al. (2023) sample includes G19.01–0.03 MM1, and their values for the CH_3OCH_3 , CH_3OCHO and CH_3CHO column densities towards MM1 – derived using LTE synthetic spectra – are within a factor of 2–4 of the order of magnitude estimates in Table 7. We note that, for consistency, we do not include data points from Chen et al. (2023) in Fig. 13 because they derive CH_3OH column densities from modelling of the $\text{CH}_3^{18}\text{OH}$ isotopologue and an assumed $^{16}\text{O}/^{18}\text{O}$ isotope ratio, and do not derive $T_{\text{CH}_3\text{OH}}$ values for most (13/14) of the sources in their sample.

It is worth emphasizing that comparisons of column densities are subject to a number of varying effects including beam sizes, source distance and beam dilution. The sources collated here, despite all being observed with ALMA, appear to trace different spatial scales across mass. The low-mass data probe physical scales of 13–140 au (physical scale of the synthesized beam; median and standard deviation of 60 and 40 au, respectively), a factor of up to two orders of magnitude smaller than the 400–2600 au spatial scales (physical scale of the synthesized beam; median and standard deviation of 990 and 870 au, respectively) probed by the high-mass data. It is suggested by van Gelder et al. (2022) that methanol production could be less efficient towards MYSOs due to their warmer pre-stellar phase and/or shorter pre-stellar lifetimes. Nazari, Tabone & Rosotti (2023) model the methanol emission towards different configuration high-mass sources. Comparing their results to a similar study of theirs towards low-mass sources (Nazari et al. 2022), they find that optically thick millimetre dust, as well as disc shadowing causing a reduction in environment temperature, are more effective in lowering the methanol emission towards low-mass YSOs than they are towards MYSOs with high luminosity ($10^4 - 10^5 L_\odot$). It is therefore further suggested by Nazari et al. (2023) that other factors such as the presence of HII regions, could contribute to the lowering of methanol emission towards some MYSOs. It is possible a combination of these factors could be contributing to the methanol column densities, temperature and fractional abundances appearing so similar across mass scales in Fig. 13. It may also be explained by considering the conditions under which these COMs are formed. Recent works have suggested that the chemical similarity between various sources may be explained by the COMs being formed under similar conditions (e.g. Quénard et al. 2018). Across mass scales this would correspond to the ices of the pre-stellar phase (e.g. Coletta et al. 2020; Nazari et al. 2022; Chen et al. 2023).

In addition to CH_3OCH_3 and CH_3CHO , Csengeri et al. (2019) also report the fractional abundances of CH_3OCHO , $\text{CH}_3\text{CH}_2\text{OH}$ and $\text{CH}_3\text{CH}_2\text{CN}$ with respect to CH_3OH towards three positions around the high-mass hot core G328.2551–0.5321. In every instance, the corresponding molecular abundance reported here towards MM1 is of the same order as those towards G328.2551–0.5321. Cyganowski et al. (2011a) find a CH_3CN column density towards MM1 of $1.7 \times 10^{16} \text{ cm}^{-2}$ with their SMA 1.3 mm observations (with $32 \times$ larger beam area than our ALMA data). They also find that the CH_3CN spectrum is best-fit by a model with a CH_3CN -emitting region of size 0.6 arcsec (equivalent to 2400 au at $D = 4 \text{ kpc}$), intermediate between our ALMA beam (Table 1) and the size of the MM1 1.05 mm dust continuum from Table 3. Nazari et al. (2022) present CH_3CN column densities towards 37 high-luminosity, potentially high-mass, protostars; 13 have column densities of a similar order to MM1 (Cyganowski et al. 2011a), whilst Law et al. (2021) reports a CH_3CN column density for G10.6 HC 1 an order of magnitude larger than MM1.

The comparatively weak, sparse COM emission towards MM1 in the SMA observations of Cyganowski et al. (2011a) led to the suggestion that MM1 was a relatively young source. Now, with a rich line forest detected with ALMA, and fractional abundances of COMs similar to other sources in the literature, it is clear that MM1 is not especially chemically young and in fact appears to be a typical hot core.

4.3.3 $^{12}\text{C}/^{13}\text{C}$ isotope ratio

With the identification of both the ^{12}C and ^{13}C isotopologues of CH_3OH , we can estimate the $^{12}\text{C}/^{13}\text{C}$ isotope ratio from the ratio of their column densities (see Table 7). This is valid if the molecular transitions are optically thin, described by the same rotational temperature, and exhibit similar spatial emission extents (e.g. Wirström et al. 2011). Towards the ALMA 1.05 mm continuum peak of MM1, we estimate that $^{12}\text{C}/^{13}\text{C} \simeq 6$. This is a factor of ~ 7 lower than expected from the relations of Wilson & Rood (1994) and Milam et al. (2005) for galactic molecular clouds (where $^{12}\text{C}/^{13}\text{C} \simeq 39 - 46$ at the MM1 galactocentric distance of 4.4 kpc).

Though low-J transitions of CH_3OH are commonly optically thick (e.g. Ginsburg et al. 2017), five out of the six lines included in our LTE line modelling (see Section 4.1.3) are relatively high-J transitions (see Table 4). The estimated opacities of the six lines are $\tau \sim 0.1-0.6$ based on the CLASS modelling (with an average of 0.3; see Section 4.1.3), and $\tau \sim 0.4$ to 2.1 from the rotation diagram

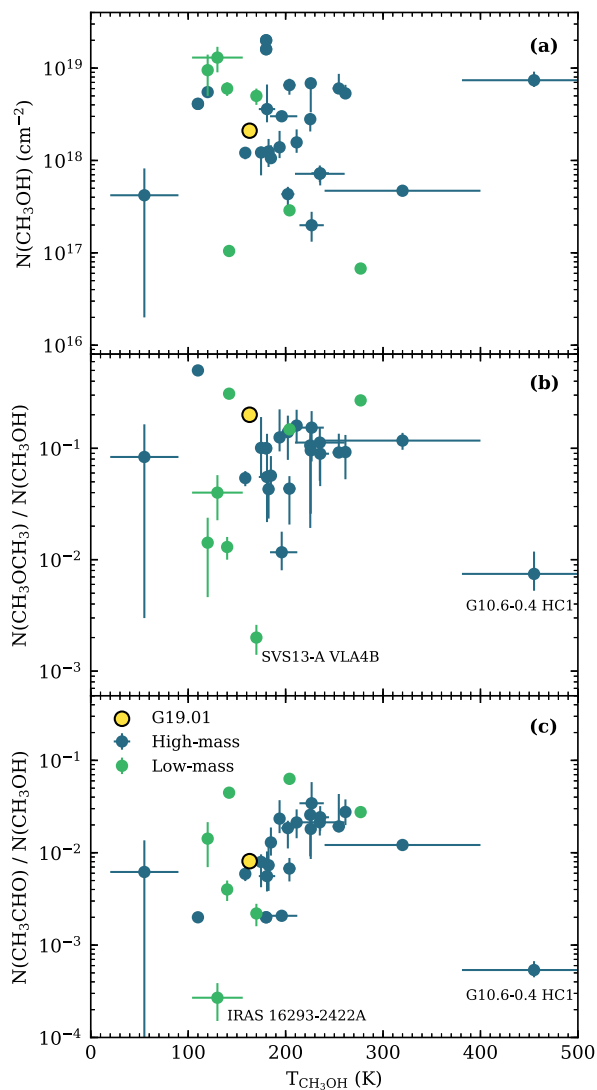


Figure 13. (a) CH_3OH column density, (b) abundance of CH_3OCH_3 with respect to CH_3OH , and (c) abundance of CH_3CHO with respect to CH_3OH , all plotted against CH_3OH rotational temperature, of both low-mass (green) and high-mass (blue) sources from the literature (inspired by Figs 7&8 of Öberg et al. 2014). Our G19.01 data is plotted in yellow. All sources were observed with ALMA: the synthesized beams of the collated low- and high-mass literature observations range from 13 to 140 au and 400 to 2600 au, respectively. High-mass sources were collated from Csengeri et al. (2019), Molet et al. (2019), Law et al. (2021) and Baek et al. (2022), and low-mass sources were collated from Lee et al. (2019), Manigand et al. (2020), Bianchi et al. (2022), Chahine et al. (2022), and Hsu et al. (2022). The G19.01 errors bars are smaller than the marker size, and not all literature sources have error bars.

analysis (with an average of 1.0; see Section 4.1.1). The opacity of the $^{13}\text{CH}_3\text{OH}(3_{2,2} - 4_{1,3})$ line reported by CLASS is $\tau = 1.0$. It is worth noting that the LTE modelling reproduces the observed emission of the highest-J and lowest- τ $^{12}\text{CH}_3\text{OH}$ line very well (i.e. $\text{CH}_3\text{OH}(23_{4,19} - 22_{5,18})$ with $\tau = 0.1$ and 0.4 from CLASS and the rotation diagram respectively), and that the spatial extent of emission from this line is consistent with that of $^{13}\text{CH}_3\text{OH}(3_{2,2} - 4_{1,3})$ (see fig. 3 of Paper I). To test for dependence on the assumed source size, we reran our WEEDSPY_MCMC analysis at the 1.05 mm continuum peak for the case of unresolved emission (source size

$0''.2$, Section 4.1.1) and re-estimated the $^{13}\text{CH}_3\text{OH}$ column density as described in Section 4.3.1 using the resulting parameters. We emphasise that the best-fitting model with this smaller source size is a poorer representation of the observed $^{12}\text{CH}_3\text{OH}$ emission than the model described in Sections 4.1.3–4.1.4, and we use it only to check the effect of the assumed source size on the $^{12}\text{C}/^{13}\text{C}$ ratio. From the models with a $0''.2$ source size, we derive a $^{12}\text{C}/^{13}\text{C}$ ratio of ~ 7.5 , indicating that the result of low $^{12}\text{C}/^{13}\text{C}$ is robust to the assumption of resolved or unresolved emission.

There are suggestions in the literature that $^{12}\text{C}/^{13}\text{C}$ may be generally lower on the smaller scales of high-mass hot cores (e.g. IRAS 20126+4104, G31.41–0.31, AFGL 4176, W3 IRS4, and G10.6–0.4; Palau et al. 2017; Beltrán et al. 2018; Bøgelund et al. 2019; Mottram et al. 2020; Law et al. 2021, respectively) and low-mass hot corinos (Hsu et al. 2022) than on the larger scale of molecular clouds. Proposed chemical explanations include cold temperature enhancement of ^{13}C in H_2CO formation on dust grains (Mottram et al. 2020) and the destruction of HC_3N in chemical reactions (Bøgelund et al. 2019). The possible contribution of optical depth effects has also been considered (Beltrán et al. 2018; Bøgelund et al. 2019; Law et al. 2021). Beltrán et al. (2018) and Bøgelund et al. (2019) conduct synthetic analyses of CH_3CN and HC_3N emission, respectively (taking similar approaches to that detailed here towards G19.01), and comment that optically thick emission could artificially lower their observed $^{12}\text{C}/^{13}\text{C}$ ratios. Law et al. (2021) conclude that optical depth effects are unlikely to drive their results as $\tau \sim 0.1$ – 0.4 for their CH_3OH lines (derived using a rotation diagram analysis), but note they cannot definitively discount optical depth effects in unresolved structures contributing to their results.

Similarly to Law et al. (2021), our derived line opacities are not suggestive of optical depth being the primary explanation for the low $^{12}\text{C}/^{13}\text{C}$ ratio observed in G19.01, but we cannot rule out optical depth effects contributing to this result. We emphasize that our observations provide only a tentative addition to the emerging picture of low $^{12}\text{C}/^{13}\text{C}$ isotope ratios towards hot cores. Observations of additional and optically thin transitions of the $^{12}\text{CH}_3\text{OH}$ and $^{13}\text{CH}_3\text{OH}$ isotopologues, as well as the isotopologues of other molecular species, would be required for confirmation.

5 CONCLUSIONS

In this paper (Paper II), we have presented a study of the physical properties and chemistry of the high-mass (proto)star G19.01–0.03 MM1 and its environment, using sub-arcsec-resolution ALMA 1.05 mm and VLA 1.21 cm data. Our main findings are as follows:

(i) A (sub)millimetre forest of molecular line emission is observed towards MM1. We analyse 47 lines from 11 different species (43 of which were identified in our ALMA 1.875 GHz wide-bands alone), including COMs such as CH_3OCHO , $\text{CH}_3\text{CH}_2\text{CN}$, $\text{CH}_3\text{CH}_2\text{OH}$, CH_3OCH_3 , NH_2CHO , and CH_3OH .

(ii) A Bayesian analysis (using our publicly available WEEDSPY_MCMC scripts) of CH_3OH LTE synthetic spectra towards the MM1 dust peak returns highest likelihood column density and temperature of $(2.22 \pm 0.01) \times 10^{18} \text{ cm}^{-2}$ and $162.7_{-0.5}^{+0.3} \text{ K}$, respectively. These are consistent with high-mass hot core sources from the literature and with values found from our opacity-corrected rotation diagram analysis of $(2.0 \pm 0.4) \times 10^{18} \text{ cm}^{-2}$ and $166 \pm 9 \text{ K}$ respectively.

(iii) The peak CH₃OH temperature (165.5 ± 0.6 K) is offset from the MM1 dust peak by 0.22 arcsec \sim 880 au. The morphology of the region of elevated temperature is aligned with the VLA 5.01 cm continuum emission presented in [Paper I](#).

(iv) We report abundances of all identified molecular species (CH₃OCH₃, ¹³CH₃OH, CH₃CH₂OH, CH₃OCHO, OCS, H₂CO, CH₃CHO, H₂CS, CH₃CH₂CN, NH₂CHO, HC₃N, and ¹³CS) of 10^{-1} – 10^{-4} and 10^{-6} – 10^{-9} with respect to CH₃OH and H₂, respectively, consistent with high-mass hot core sources from the literature.

(v) The known bipolar molecular outflow driven by MM1 is traced by thermal CH₃OH and H₂CO emission and by newly identified NH₃(3,3) and 278.3 GHz Class I CH₃OH maser candidates, strengthening the connection of these types of masers with outflows driven by MYSOs. We identify a total of 50 $> 5\sigma$ NH₃(3,3) emission spots across eight compact emission groups, which are in the outer lobes of the outflow and spatially and kinematically coincident with 44 GHz Class I CH₃OH masers. Candidate 25 GHz CH₃OH 5(2,3)-5(1,4) maser emission is also detected towards the outflow, offset from MM1 by 6 arcsec \sim 24 000 au.

(vi) Four new millimetre continuum sources (MM2...MM5) are detected between 0.03 – 0.12 pc from MM1, but all are undetected in NH₃($J = K = 1, 2, 3, 5, 6,$ and 7) and 25 GHz CH₃OH emission. Two of these sources, MM2 and MM4, are associated with $>5\sigma$ DCN(4–3) emission, a tracer of cold and dense gas.

(vii) The median mass of MM2..MM5 (assuming isothermal dust emission) is 1.0–2.0 M_⊙ for a temperature range of 24–15 K, and their median radius is \sim 2000 au. Since none of these sources are associated with any masers or have any sign of outflows, they are candidate low-mass pre-stellar companions to MM1.

In all, our results place G19.01–0.03 MM1 as a typical high-mass hot core source, with four low-mass, potentially pre-stellar, cores within a projected linear distance of 0.12 pc. Both these findings are in contrast with the results of previous, lower-resolution SMA observations (Cyganowski et al. 2011a), which identified G19.01–0.03 MM1 as a candidate for isolated high-mass star formation, potentially at a very early stage due to its lack of chemical complexity. Our new results show that G19.01–0.03 MM1 is in fact not especially chemically young, and that its physical and chemical properties are typical of other high-mass hot core sources in the literature. Intriguingly, our analysis of the ALMA CH₃OH lines reveals a region of elevated CH₃OH temperature that is aligned with VLA 5.01 cm continuum emission attributed to free–free emission, which is offset from the thermal dust emission peak (as discussed in detail in [Paper I](#)). This positional coincidence is tentative support for the possibility, suggested in [Paper I](#), that the 5.01 cm continuum might be associated with an unresolved high-mass binary companion to MM1. Our ALMA Cycle 6 follow-up study, tuned to probe \sim 0.09 arcsec \sim 360 au scales, will be a next step in testing this possibility with higher angular resolution observations.

ACKNOWLEDGEMENTS

We thank the anonymous referee for their constructive report and comments that helped improve the quality of this paper. GMW and CJC thank Ian Bonnell for helpful discussions. GMW acknowledges support from the UK's Science and Technology Facilities Council (STFC) under ST/W00125X/1. CJC acknowledges support from the UK's STFC under ST/M001296/1. PN acknowledges support by grant 618.000.001 from the Dutch Research Council (NWO) and support by the Danish National Research Foundation through the Center of Excellence 'InterCat' (Grant agreement no.: DNR150). This research has made use of: NASA's Astrophysics Data System

Bibliographic Services, GILDAS (<https://www.iram.fr/IRAMFR/GILDAS>) and PYTHON packages ASTROPY (Astropy Collaboration 2013), ASTRODENDRO (Rosolowsky et al. 2008), APLPY (<http://apipy.github.com>), CMOCEAN (Thyng et al. 2016), CORNER (Foreman-Mackey 2016), EMCEE (Foreman-Mackey et al. 2013), MATPLOTLIB (Hunter 2007), NUMPY (Harris et al. 2020), PANDAS (McKinney 2010), SCIPY (Virtanen et al. 2020), SCITKIT-IMAGE (Van der Walt et al. 2014), and ANALYSISUTILS (Hunter et al. 2023). This paper makes use of the following ALMA data: ADS/JAO.ALMA#2013.1.00812.S. ALMA is a partnership of ESO (representing its member states), NSF (USA) and NINS (Japan), together with NRC (Canada), NSC and ASIAA (Taiwan), and KASI (Republic of Korea), in cooperation with the Republic of Chile. The Joint ALMA Observatory is operated by ESO, AUI/NRAO, and NAOJ. The National Radio Astronomy Observatory is a facility of the National Science Foundation operated under cooperative agreement by Associated Universities, Inc. For the purposes of open access, the author has applied a Creative Commons Attribution (CC BY) licence to any Author Accepted Manuscript version arising.

DATA AVAILABILITY

The ALMA 1.05 mm dust continuum, VLA 1.21 and 5.01 cm continuum images, and the line cubes for the two broad (1.875 GHz bandwidth) ALMA spectral windows are available at doi:10.5281/zenodo.8059531. These data underlie both this article and Williams et al. (2022). The scripts used to conduct the Bayesian analysis of LTE synthetic spectra are packaged together in a reusable form we call WEEDSPY_MCMC, and are made freely available at https://github.com/gwen-williams/WeedsPy_MCMC.

REFERENCES

- Astropy Collaboration, 2013, *A&A*, 558, A33
 Baek G., Lee J.-E., Hirota T., Kim K.-T., Kyoung Kim M., 2022, *ApJ*, 939, 84
 Barnes A. T. et al., 2023, *A&A*, 675, A53
 Beltrán M. T. et al., 2014, *A&A*, 571, A52
 Beltrán M. T. et al., 2018, *A&A*, 615, A141
 Bertoldi F., McKee C. F., 1992, *ApJ*, 395, 140
 Beuther H., Schilke P., Gueth F., McCaughrean M., Andersen M., Sridharan T. K., Menten K. M., 2002, *A&A*, 387, 931
 Bianchi E., López-Sepulcre A., Ceccarelli C., Codella C., Podio L., Bouvier M., Enrique-Romero J., 2022, *ApJ*, 928, L3
 Billington S. J. et al., 2020, *MNRAS*, 499, 2744
 Bøgelund E. G., Barr A. G., Taquet V., Ligterink N. F. W., Persson M. V., Hogerheijde M. R., van Dishoeck E. F., 2019, *A&A*, 628, A2
 Bonnell I. A., Bate M. R., Clarke C. J., Pringle J. E., 2001, *MNRAS*, 323, 785
 Brogan C. L., Chandler C. J., Hunter T. R., Shirley Y. L., Sarma A. P., 2007, *ApJ*, 660, L133
 Brogan C. L., Hunter T. R., Cyganowski C. J., Indebetouw R., Beuther H., Menten K. M., Thorwirth S., 2009, *ApJ*, 707, 1
 Brogan C. L., Hunter T. R., Cyganowski C. J., Friesen R. K., Chandler C. J., Indebetouw R., 2011, *ApJ*, 739, L16
 Brogan C. L., Hunter T. R., Cyganowski C. J., Chandler C. J., Friesen R., Indebetouw R., 2016, *ApJ*, 832, 187
 Brogan C. L. et al., 2019, *ApJ*, 881, L39
 Cesaroni R. et al., 2017, *A&A*, 602, A59
 Chahine L. et al., 2022, *A&A*, 657, A78
 Chen Y. et al., 2023, preprint ([arXiv:2308.02688](https://arxiv.org/abs/2308.02688))
 Chevance M. et al., 2020, *MNRAS*, 493, 2872
 Coletta A., Fontani F., Rivilla V. M., Minnini C., Colzi L., Sánchez-Monge Á., Beltrán M. T., 2020, *A&A*, 641, A54

- Csengeri T., Belloche A., Bontemps S., Wyrowski F., Menten K. M., Bouscasse L., 2019, *A&A*, 632, A57
- Cummins S. E., Linke R. A., Thaddeus P., 1986, *ApJS*, 60, 819
- Cyganowski C. J. et al., 2008, *AJ*, 136, 2391
- Cyganowski C. J., Brogan C. L., Hunter T. R., Churchwell E., 2009, *ApJ*, 702, 1615
- Cyganowski C. J., Brogan C. L., Hunter T. R., Churchwell E., Zhang Q., 2011a, *ApJ*, 729, 124
- Cyganowski C. J., Brogan C. L., Hunter T. R., Churchwell E., 2011b, *ApJ*, 743, 56
- Cyganowski C. J., Koda J., Rosolowsky E., Towers S., Donovan Meyer J., Egusa F., Momose R., Robitaille T. P., 2013, *ApJ*, 764, 61
- Cyganowski C. J. et al., 2014, *ApJ*, 796, L2
- Cyganowski C. J., Brogan C. L., Hunter T. R., Smith R., Kruijssen J. M. D., Bonnell I. A., Zhang Q., 2017, *MNRAS*, 468, 3694
- Cyganowski C. J., Hannaway D., Brogan C. L., Hunter T. R., Zhang Q., 2018, in Tarchi A., Reid M. J., Castangia P., eds, *Proc. IAU Symp.* 336, *Astrophysical Masers: Unlocking the Mysteries of the Universe*. Cambridge Univ. Press, p. 281
- Cyganowski C. J., Ilee J. D., Brogan C. L., Hunter T. R., Zhang S., Harries T. J., Haworth T. J., 2022, *ApJ*, 931, L31
- Dewangan L. K. et al., 2022, *ApJ*, 925, 41
- Duarte-Cabral A., Bontemps S., Motte F., Hennemann M., Schneider N., André P., 2013, *A&A*, 558, A125
- Duarte-Cabral A., Bontemps S., Motte F., Gusdorf A., Csengeri T., Schneider N., Louvet F., 2014, *A&A*, 570, A1
- Dullemond C. P. et al., 2018, *ApJ*, 869, L46
- Elia D. et al., 2017, *MNRAS*, 471, 100
- Foreman-Mackey D., 2016, *J. Open Source Softw.*, 1, 24
- Foreman-Mackey D., Hogg D. W., Lang D., Goodman J., 2013, *PASP*, 125, 306
- Forgan D. H., Ilee J. D., Cyganowski C. J., Brogan C. L., Hunter T. R., 2016, *MNRAS*, 463, 957
- Garrod R. T., 2013, *ApJ*, 765, 60
- Garrod R. T., Herbst E., 2006, *A&A*, 457, 927
- Garrod R. T., Jin M., Matis K. A., Jones D., Willis E. R., Herbst E., 2022, *ApJS*, 259, 1
- Ginsburg A. et al., 2017, *ApJ*, 842, 92
- Goldsmith P. F., Langer W. D., 1999, *ApJ*, 517, 209
- Goodman J., Weare J., 2010, *Commun. Appl. Math. Comput. Sci.*, 5, 65
- Grudić M. Y., Guszejnov D., Offner S. S. R., Rosen A. L., Raju A. N., Faucher-Giguère C.-A., Hopkins P. F., 2022, *MNRAS*, 512, 216
- Harris C. R. et al., 2020, *Nature*, 585, 357
- He J. H., Takahashi S., Chen X., 2012, *ApJS*, 202, 1
- Herbst E., van Dishoeck E. F., 2009, *ARA&A*, 47, 427
- Herschel Explanatory Supplement Volume III, 2017, in PACS Handbook, 2.0 edn. Available at: <https://www.cosmos.esa.int/web/herschel/legacy-documentation>
- Hildebrand R. H., 1983, *QJRAS*, 24, 267
- Hoare M. G. et al., 2005, in Cesaroni R., Felli M., Churchwell E., Walmsley M., eds, *Proc. IAU Symp.* 227, *Massive Star Birth: A Crossroads of Astrophysics*. Cambridge Univ. Press, p. 370
- Hsu S.-Y. et al., 2022, *ApJ*, 927, 218
- Huang J. et al., 2018, *ApJ*, 869, L42
- Hunter J. D., 2007, *Comput. Sci. Eng.*, 9, 90
- Hunter T. R. et al., 2018, *ApJ*, 854, 170
- Hunter T. R., Petry D., Barkats D., Corder S., Indebetouw R., 2023, *analysisUtils*, *Zenodo*, available at: doi:10.5281/zenodo.7502160
- Ilee J. D., Cyganowski C. J., Nazari P., Hunter T. R., Brogan C. L., Forgan D. H., Zhang Q., 2016, *MNRAS*, 462, 4386
- Issac N., Tej A., Liu T., Varricatt W., Vig S., Ishwara Chandra C. H., Schultheis M., Nandakumar G., 2020, *MNRAS*, 497, 5454
- Johnston K. G. et al., 2015, *ApJ*, 813, L19
- Jones B. M. et al., 2020, *MNRAS*, 493, 2015
- Kauffmann J., Bertoldi F., Bourke T. L., Evans N. J. I., Lee C. W., 2008, *A&A*, 487, 993
- Kauffmann J., Pillai T., Goldsmith P. F., 2013, *ApJ*, 779, 185
- Kim J. et al., 2021, *MNRAS*, 504, 487
- Kong S., Tan J. C., Caselli P., Fontani F., Liu M., Butler M. J., 2017, *ApJ*, 834, 193
- Kraemer K. E., Jackson J. M., 1995, *ApJ*, 439, L9
- Kratter K., Lodato G., 2016, *ARA&A*, 54, 271
- Kurtz S., 2005, in Cesaroni R., Felli M., Churchwell E., Walmsley M., eds, *Proc. IAU Symp.* 227, *Massive Star Birth: A Crossroads of Astrophysics*. Cambridge Univ. Press, p. 111
- Law C. J., Zhang Q., Öberg K. I., Galván-Madrid R., Keto E., Liu H. B., Ho P. T. P., 2021, *ApJ*, 909, 214
- Law C.-Y. et al., 2022, *ApJ*, 939, 120
- Lee C.-F., Codella C., Li Z.-Y., Liu S.-Y., 2019, *ApJ*, 876, 63
- Liu H.-L. et al., 2021, *MNRAS*, 505, 2801
- MacLaren I., Richardson K. M., Wolfendale A. W., 1988, *ApJ*, 333, 821
- Mangum J. G., Wootten A., 1994, *ApJ*, 428, L33
- Manigand S. et al., 2020, *A&A*, 635, A48
- Maret S., Hily-Blant P., Pety J., Bardeau S., Reynier E., 2011, *A&A*, 526, A47
- Maud L. T. et al., 2018, *A&A*, 620, A31
- McGuire B. A. et al., 2018, *ApJ*, 863, L35
- McKee C. F., Tan J. C., 2003, *ApJ*, 585, 850
- McKinney W., 2010, in van der Walt S., Millman J., eds, *Proc. 9th Python in Sci. Conf.: Data Structures for Statistical Computing in Python*. p. 56
- Mignon-Risse R., González M., Commerçon B., 2021, *A&A*, 656, A85
- Milam S. N., Savage C., Brewster M. A., Ziurys L. M., Wyckoff S., 2005, *ApJ*, 634, 1126
- Molet J. et al., 2019, *A&A*, 626, A132
- Morii K. et al., 2021, *ApJ*, 923, 147
- Motte F., Bontemps S., Schilke P., Schneider N., Menten K. M., Brogière D., 2007, *A&A*, 476, 1243
- Motte F., Bontemps S., Louvet F., 2018, *ARA&A*, 56, 41
- Mottram J. C. et al., 2011, *ApJ*, 730, L33
- Mottram J. C. et al., 2020, *A&A*, 636, A118
- Müller H. S. P., Thorwirth S., Roth D. A., Winnewisser G., 2001, *A&A*, 370, L49
- Müller H. S. P., Menten K. M., Mäder H., 2004, *A&A*, 428, 1019
- Müller H. S. P., Schlöder F., Stutzki J., Winnewisser G., 2005, *J. Mol. Struct.*, 742, 215
- Nazari P. et al., 2022, *A&A*, 668, A109
- Nazari P., Tabone B., Rosotti G. P., 2023, *A&A*, 671, A107
- Nony T. et al., 2018, *A&A*, 618, L5
- Öberg K. I., 2016, *Chem. Rev.*, 116, 9631
- Öberg K. I., Fayolle E. C., Reiter J. B., Cyganowski C., 2014, *Faraday Discuss.*, 168, 81
- Ossenkopf V., Henning T., 1994, *A&A*, 291, 943
- Palau A. et al., 2015, *MNRAS*, 453, 3785
- Palau A. et al., 2017, *MNRAS*, 467, 2723
- Palau A. et al., 2021, *ApJ*, 912, 159
- Parise B., Leurini S., Schilke P., Roueff E., Thorwirth S., Lis D. C., 2009, *A&A*, 508, 737
- Peretto N., Fuller G. A., 2009, *A&A*, 505, 405
- Peters T. et al., 2017, *MNRAS*, 466, 3293
- Pickett H. M., Poynter R. L., Cohen E. A., Delitsky M. L., Pearson J. C., Müller H. S. P., 1998, *J. Quant. Spectrosc. Radiat. Transfer*, 60, 883
- Pillai T., Wyrowski F., Carey S. J., Menten K. M., 2006, *A&A*, 450, 569
- Poglitsch A. et al., 2010, *A&A*, 518, L2
- Purcell C. R., Longmore S. N., Burton M. G., Walsh A. J., Minier V., Cunningham M. R., Balasubramanyam R., 2009, *MNRAS*, 394, 323
- Quénard D., Jiménez-Serra I., Viti S., Holdship J., 2018, *IAU Symp.*, 332, 415
- Rathborne J. M., Jackson J. M., Simon R., 2006, *ApJ*, 641, 389
- Redaelli E., Bovino S., Sanhueza P., Morii K., Sabatini G., Caselli P., Giannetti A., Li S., 2022, *ApJ*, 936, 169
- Reid M. J. et al., 2014, *ApJ*, 783, 130
- Rosen A. L., Krumholz M. R., 2020, *AJ*, 160, 78
- Rosolowsky E. W., Pineda J. E., Kauffmann J., Goodman A. A., 2008, *ApJ*, 679, 1338
- Rosolowsky E. et al., 2010, *ApJS*, 188, 123
- Sánchez-Monge Á. et al., 2017, *A&A*, 604, A6

- Sanhueza P., Jackson J. M., Foster J. B., Garay G., Silva A., Finn S. C., 2012, *ApJ*, 756, 60
- Sanhueza P. et al., 2019, *ApJ*, 886, 102
- Schuller F. et al., 2009, *A&A*, 504, 415
- Sewilo M. et al., 2018, *ApJ*, 853, L19
- Smith R. J., Longmore S., Bonnell I., 2009, *MNRAS*, 400, 1775
- Tan J. C., Beltrán M. T., Caselli P., Fontani F., Fuente A., Krumholz M. R., McKee C. F., Stolte A., 2014, in Beuther H., Klessen R. S., Dullemond C. P., Henning T., eds, *Protostars and Planets VI*. Univ. Arizona Press, Tucson, p. 149
- Thyng K. M., Greene C. A., Hetland R. D., Zimmerle H. M., DiMarco S. F., 2016, *Oceanography*, 29, 3
- Towner A. P. M., Brogan C. L., Hunter T. R., Cyganowski C. J., McGuire B. A., Indebetouw R., Friesen R. K., Chandler C. J., 2017, *ApJS*, 230, 22
- Towner A. P. M., Brogan C. L., Hunter T. R., Cyganowski C. J., 2021, *ApJ*, 923, 263
- Townes C. H., Schawlow A. L., 1955, *Microwave Spectroscopy*. McGraw-Hill Inc., US
- Urquhart J. S., Hoare M. G., Lumsden S. L., Oudmaijer R. D., Moore T. J. T., 2008, in Beuther H., Linz H., Henning T., eds, *ASP Conf. Ser. Vol. 387, Massive Star Formation: Observations Confront Theory*. Astron. Soc. Pac., San Francisco, p. 381
- Urquhart J. S. et al., 2011, *MNRAS*, 418, 1689
- Urquhart J. S. et al., 2013, *MNRAS*, 431, 1752
- van Gelder M. L. et al., 2022, *A&A*, 662, A67
- Virtanen P. et al., 2020, *Nat. Methods*, 17, 261
- Voronkov M. A., Caswell J. L., Ellingsen S. P., Breen S. L., Britton T. R., Green J. A., Sobolev A. M., Walsh A. J., 2012, in Booth R. S., Vlemmings W. H. T., Humphreys E. M. L., eds, *Proc. IAU Symposium 287, Cosmic Masers—from OH to H0*. p. 433
- Van der Walt S. et al., 2014, *PeerJ*, 2, e453
- Wang K., Zhang Q., Wu Y., Li H.-b., Zhang H., 2012, *ApJ*, 745, L30
- Wang K. et al., 2014, *MNRAS*, 439, 3275
- Ward-Thompson D., Scott P. F., Hills R. E., Andre P., 1994, *MNRAS*, 268, 276
- Wielen M., Wyrowski F., Schuller F., Menten K. M., Walmsley C. M., Bronfman L., Motte F., 2012, *A&A*, 544, A146
- Williams G. M. et al., 2022, *MNRAS*, 509, 748
- Wilson T. L., Rood R., 1994, *ARA&A*, 32, 191
- Wirström E. S. et al., 2011, *A&A*, 533, A24
- Wu Y. W. et al., 2014, *A&A*, 566, A17
- Yanagida T. et al., 2014, *ApJ*, 794, L10
- Yang A. Y., Thompson M. A., Tian W. W., Bihl S., Beuther H., Hindson L., 2019, *MNRAS*, 482, 2681
- Yang A. Y. et al., 2021, *A&A*, 645, A110
- Yang A. Y. et al., 2022, *A&A*, 658, A160
- Zhang Q., Sridharan T. K., Hunter T. R., Chen Y., Beuther H., Wyrowski F., 2007, *A&A*, 470, 269

APPENDIX A: $N_2H^+(3-2)$ ABSORPTION TOWARDS MM1

Fig. A1 shows the $N_2H^+(3-2)$ spectrum towards the MM1 ALMA 1.05 mm continuum peak, extracted from the continuum-subtracted line image cube. As shown in Fig. A1, the deepest absorption (at $\sim 58 \text{ km s}^{-1}$) is blue-shifted relative to the systemic velocity of MM1 measured from its hot-core line emission ($59.9 \pm 1.1 \text{ km s}^{-1}$; Cyganowski et al. 2011a).

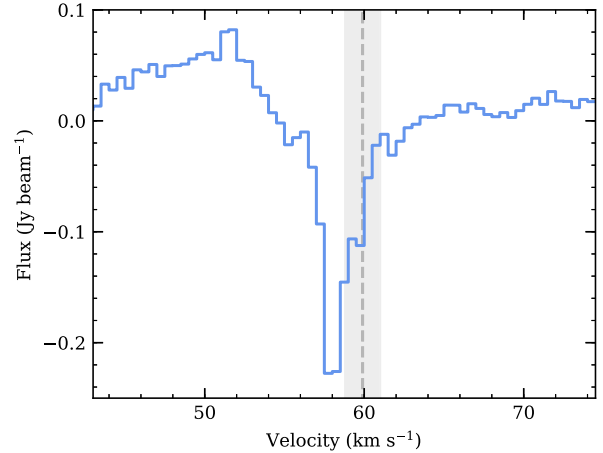


Figure A1. $N_2H^+(3-2)$ spectrum towards the ALMA 1.05 mm continuum peak of MM1. The systemic velocity of MM1 ($59.9 \pm 1.1 \text{ km s}^{-1}$; Cyganowski et al. 2011a) is marked by the vertical grey dashed line (with the uncertainty represented by the shaded region).

APPENDIX B: CONVERGENCE OF WALKERS IN WEEDSPY_MCMC ANALYSIS OF LTE SYNTHETIC SPECTRA

In Section 4.1.2, we used the PYTHON package EMCEE to sample the parameter space of the LTE synthetic spectra produced by the Weeds package of the CLASS software. Here, we discuss how we heuristically assessed algorithm parameters.

We ran a number of tests on the spectrum at the peak ALMA 1.05 mm continuum pixel of MM1, with varying numbers of walkers and iterations. Fig. B1 shows an example trace plot for the chains (i.e. walked paths) of 60 initiated walkers, allowed to walk for a total of 700 iterations each. We find that 200 burn-in iterations is sufficient for the walkers to locate the regions of highest probability in the parameter space. Since our analysis towards MM1 requires running this analysis on ~ 120 observed spectra, our choice of production run iterations is mostly motivated by computational time constraints. For 500 production run iterations, the analysis for one spectrum takes 30 min to complete. To assess whether this is appropriate or not, we calculate the acceptance fraction (a_f) and the integrated autocorrelation time (τ_{ac}). The acceptance fraction describes the fraction of iterations that were accepted, while the autocorrelation time describes the number of iterations the sampler takes to draw independent samples (i.e. effectively the number of iterations it takes to forget where the walkers were initialized). Good samplers are generally quoted to have $a_f = 0.2-0.5$ (e.g. Foreman-Mackey et al. 2013), while the lower the autocorrelation time the better. We calculate a mean τ_{ac} over 500 production iterations of 45, 50, 60, and 35 iterations for the four free parameters of the model, respectively. Foreman-Mackey et al. (2013), however, recommend that the number of production iterations should be at least $50\tau_{ac}$. This would require 3000 production iterations, a six-fold increase on the 500 iterations shown in Fig. B1, resulting in a computational time cost across all 120 spectra of more than 2 weeks. This was unrealistic for our analysis. However, it is encouraging that the burn-in iterations are seen to be a number of multiples of the estimated τ_{ac} (between 3 and 6), and that the production iterations successfully focus on the region of highest probability (as seen in Fig. B1). As convergence of such a sampler is

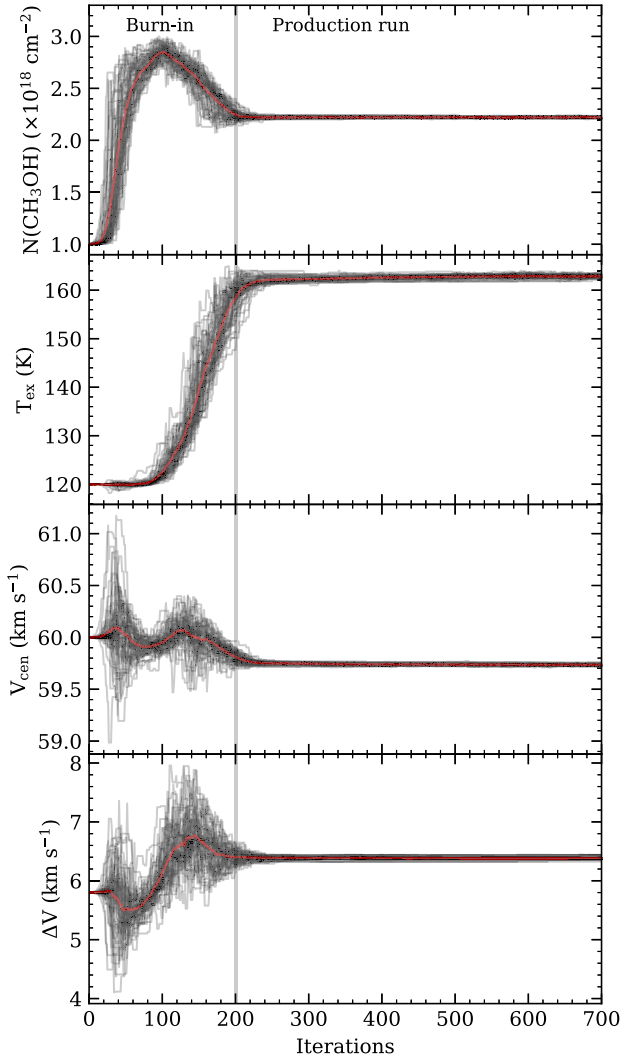


Figure B1. Trace plots of the chains of 60 walkers across the four free parameters of the analysis (column density, temperature, centroid velocity, and velocity width), for the total number of 700 iterations, evaluated for the spectrum towards the peak position of the ALMA 1.05 mm continuum emission of MM1. The running mean is overplotted in red in each panel. The sampler was allowed to ‘burn-in’ for the first 200 iterations (marked by the vertical grey line), after which a further 500 ‘production’ iterations were run.

always a non-trivial metric to estimate, and given that our estimated $a_f = 0.21$ is just within the typically quoted acceptable range from the literature, we consider that for all intents and purposes these chains are ‘converged’, with final highest likelihood results that are valid within the confidence intervals of the normally distributed posterior distributions shown in Fig. 10. Only the posterior distribution for the velocity width in Fig. 10 does not appear normally distributed, as mentioned in Section 4.1.2. Though the statistical error on the velocity width is significantly lower than the spectral resolution of the data, this motivated a final test where we initialized the 60 walkers with a different random number seed. This yielded very similar chain traces and posterior distributions, giving confidence that the final result is independent of initial walker position.

This paper has been typeset from a \LaTeX file prepared by the author.